J. Fluid Mech. (2004), *vol.* 512, *pp.* 313–341.
DOI: 10.1017/S0022112004009851 Printed in the United Kingdom

Investigation of flow over an oscillating airfoil

By T. LEE AND P. GERONTAKOS

Department of Mechanical Engineering, McGill University, Montreal, Canada H3A 2K6

(Received 7 October 2002 and in revised form 19 April 2004)

The characteristics of the unsteady boundary layer and stall events occurring on an oscillating NACA 0012 airfoil were investigated by using closely spaced multiple hot-film sensor arrays at $Re = 1.35 \times 10^5$. Aerodynamic forces and pitching moments, integrated from surface pressure measurements, and smoke-flow visualizations were also obtained to supplement the hot-film measurements. Special attention was focused on the behaviour of the spatial-temporal progression of the locations of the boundary-layer transition and separation, and reattachment and relaminarization points, compared to the static values, for a range of oscillation frequency and amplitude both prior to, during and after the stall. The initiation, growth and rearward convection of a leading-edge vortex, and the role of the laminar separation bubble leading to the dynamic stall, as well as the mechanisms responsible for the stall events observed at different test conditions were also characterized. The hot-film measurements were also correlated with the aerodynamic load and pitching moment results to quantify the values of lift increment and stall angle delay as a result of the observed boundary layer and stall events. The results reported here provide an insight into the detailed nature of the unsteady boundary-layer events as well as the stalling mechanisms at work at different stages in the dynamic-stall process.

1. Introduction

The phenomenon of dynamic stall on airfoils and lifting surfaces in unsteady flow environments has been studied for many years, both as an important practical problem and as a challenging fundamental one as well. The effects of unsteady motion on aircraft stall characteristics, especially on the dynamic retreating blade stall problems of helicopters, a well-known limiting factor for the high-speed performance of modern helicopters that accompanies high lift and torsional loadings, have been recognized and received considerable attention. Numerous experimental and computational investigations (for example, Johnson & Ham 1972; Martin *et al.* 1974; McCroskey & Philippe 1975; McCroskey, Carr & McAlister 1976; Carr, McAlister & McCroskey 1977; McAlister, Carr & McCroskey 1978; McCroskey *et al.* 1981; Chow & Chiu 1986; Jumper, Schreck & Dimmick 1987; Ericsson & Reding 1988; Jumper 1988; Jumper, Dimmick & Allaire 1989; Park, Kim & Lee 1989; Srinivassan, Ekaterinaris & McCroskey 1993; Schreck, Faller & Helin 1994; Chandrasekhara & Carr 1990; Lober, Carta & Covino 1992; Panda & Zaman 1994; Ko & McCroskey 1997; Lee & Basu 1998) have shown that the unsteady flow can be separating or reattaching over a large portion of the top surface of the airfoil, and that the predominant feature of dynamic stall is the formation and shedding and convection over the upper surface of the airfoil of an energetic vortex-like disturbance from the leading edge of the airfoil, which induces a nonlinearly fluctuating pressure field and produces transient variations in forces and moments that are fundamentally different from their

steady-state counterparts. After the leading-edge vortex passes the airfoil trailing edge and goes into the wake, the flow progresses to a state of full separation over the upper surface. This is accompanied by a sudden loss of lift and a decrease in pitching moment. Furthermore, if and when the angle of attack becomes low enough, the flow will finally reattach again from the leading edge. An excellent review on unsteady airfoils is given by McCroskey (1982). In addition, numerous new airfoil designs and control schemes have also been proposed in an attempt to improve the stall characteristics of rotors without compromising advance-blade performance (Rennie & Jumper 1996; Hsiao, Liang & Huang 1998; Nguyen 1998; Greenblatt, Neuburger & Wygnaski 2001; Magill *et al.* 2003).

Among the considerable dynamic-stall prediction efforts, Ericsson & Reding (1988) reported that for a constant-pitching NACA 0012 airfoil, the unsteady airfoil stall is characterized by two distinctly different flow phenomena: the delay of stall due to time-lag and boundary-layer-improvement effects, which is quasi-steady in nature, and the transient behaviour of the forward movement of the separation point and the following 'spillage' of a leading-edge or dynamic vortex (LEV). The time-lag effects occur before a change of flow condition can affect the separation-induced aerodynamic loads or the lag effect due to the time required to convect the boundary-layer reaction to the pressure gradient change from the leading edge to the point of separation. They suggested that the dynamic overshoot of the static-stall angle, α_{ss}, has two components: $\Delta\alpha_{t1}$ (which is purely a convective-flow time-lag effect which only displaces the static characteristic in the $\alpha(t)$ frame) and $\Delta\alpha_s = \Delta\alpha_{s1} + \Delta\alpha_{s2}$, which produces the experimentally observed large overshoot $\Delta C_{lmax} = C_{l\alpha}\Delta\alpha_s$ over the static C_{lmax}. $\Delta\alpha_{s1}$ is the stall angle increment due to the forward movement of the flow separation, and $\Delta\alpha_{s2}$ is the stall angle increment resulting from the formation and spillage of the LEV. $C_{l\alpha} = \mathrm{d}C_l/\mathrm{d}\alpha$ is the lift-curve slope. The accelerated flow and the moving wall or 'leading-edge-jet' effects, which increase the tangential wall velocities and improve the boundary-layer characteristics during the increasing-α phase of a pitching airfoil, contribute to $\Delta\alpha_{s1}$, and render a delayed flow separation and a substantial overshoot of static stall. Ericsson & Reding also suggest that when the static-stall angle has been exceeded by $\Delta\alpha_{sep} = \Delta\alpha_{t1} + \Delta\alpha_{s1}$, massive separation occurs and the following transient effects take place: the separation point moves toward the leading edge and the leading-edge vortex is 'spilled'. The formation and travel and spillage (which is associated with a discontinuous change of the circulation) of the leading-edge vortex dominate the dynamic overshoot and contribute directly to $\Delta\alpha_{s2}$. Evidently, unsteady boundary-layer separation is one of the most important features involved in the dynamic-stall phenomenon. However, the theoretical understanding of the unsteady boundary-layer separation has not explicitly touched on the dynamic-stall phenomenon. This is probably because the separation in dynamic stall is so large; the whole upper surface of the airfoil is covered with a wake in those circumstances. Furthermore, Ericsson & Reding's theoretical model did not predict the presence of a thin layer of flow reversal within a thickened turbulent boundary layer originating in the trailing-edge region, as well as the nature of the LEV prior to, during and after dynamic stall.

On the other hand, Jumper *et al.* (1987, 1989) examined the effects of the unsteadiness of the flow (neglecting the wake), the motion of the airfoil tangent to the surface (i.e. the direction of the flow), and the motion of the airfoil perpendicular to the surface (i.e. into the flow) by using a modified momentum-integral method, and validated the predicted results against the flow visualization and the surface pressure measurements. Jumper *et al.* reported that the lift coefficient, C_l, jump for an airfoil

pitching about midchord at a constant rate was determined to be

$$\Delta C_l = 3.14\dot{\alpha}_{ND}\left[1 + \tfrac{2}{3}(t/c)\right], \tag{1}$$

where $\dot{\alpha}_{ND} = (c\dot{\alpha}/2)/u_\infty$ is the non-dimensional pitching rate (the ratio of the leading-edge speed, i.e. $c\dot{\alpha}/2$, to the free-stream velocity, u_∞, for the case of an airfoil pitching about the midchord), and t/c is the airfoil thickness ratio. Also, the predicted effect of $\dot{\alpha}_{ND}$ on the lift-curve slope, $C_{l\alpha}$, for a zero thickness airfoil (flat plate) was approximated by

$$C_{l\alpha} \approx 3.6 + 2.68\exp(-\dot{\alpha}_{ND} \times 10^3/4.216). \tag{2}$$

The effect described by (1) is due to the rotation of the airfoil, and is referred to in aeroelasticity as an 'apparent camber' effect (Bisolinghoff & Ashley 1975). The effect described by (2) is due to the vortices shed into the wake causing a 'time lag', which results in a different C_l for a given α in the dynamic case than that for the steady case at the same α (i.e. the influence of apparent camber effect and the effect of the shed-vortex wake). Jumper *et al.* further concluded that the wake effect does not depend on pitch location; however, the apparent camber effect is shown to be affected by pitch location. Moreover, the momentum-integral method also allows the exploration of the effect on separation of pitch locations other than the midchord, which is of fundamental importance in the understanding and ability to predict dynamic events.

In the meantime, in order to further understand the separated flows developed on unsteady airfoils, and to continue the development and validation of predictive and computational methods, much experimental effort is centred upon the measurement of aerodynamic loads, especially the detailed analyses of aerodynamic characteristics of unsteady airfoils oscillating in the post-stall regime. Experimental techniques, such as hot-wire anemometry, single surface-mounted heated wall-shear stress gauges, laser-Doppler velocimetry (LDV), surface pressure transducers, particle image velocimetry (PIV), and various flow-visualization methods, have been used by others to investigate the various critical boundary-layer flow points and stall events, including the locations of boundary-layer transition, reattachment, separation and flow reversal, and the initiation and spread of the primary and secondary vortices, as well as the characteristics of the laminar separation bubble at both pre-stall, during stall and post-stall conditions. However, the hot-wire anemometry could be intrusive and provides only pointwise flow-field information. The single or dual heated hot-film sensors are non-intrusive and have been used primarily as a skin-friction gauge, as well as to determine stages of the transition process, which can be sensitively influenced by intrusive probe. The non-intrusive LDV system is, in general, sophisticated and relatively expensive, and could be limited to the rather poor signal-to-noise ratio and the data rate close to the solid surface. The surface pressure-orifice measurement technique has been used extensively to obtain the integrated aerodynamic loads, as well as the characterization of the unsteady boundary layer developed on an oscillating airfoil. However, the acquisition of the surface pressure distribution usually requires the fabrication of a large number of pressure orifices, and the installation of the miniature pressure transducers on the airfoil model. The PIV system provides global velocity/vorticity distributions over the airfoil model, but not the region close to the airfoil surface. Convenient and practical means capable of determining the detailed characteristics of these unsteady boundary-layer and stall events occurring on an oscillating airfoil, especially in the leading-edge region, both non-intrusively and simultaneously, are obviously desired. In addition, detailed spatial-temporal

characteristics of the unsteady boundary-layer and stall events, and the mechanisms producing the leading-edge vortex and the factors which influence them, as well as the stalling mechanism under the influence of oscillation frequency and amplitude, still demand further investigation.

The main objective of this work was to investigate the detailed behaviour of the unsteady boundary layer developed on an NACA 0012 airfoil oscillated sinusoidally at pre-stall, during stall and post-stall conditions by using closely spaced multiple hot-film sensor arrays. Surface pressure distributions, hot-wire wake measurements and smoke-flow visualizations were also obtained to supplement the hot-film data. The unique multiple hot-film sensors were used primarily to determine both non-intrusively and simultaneously the details of the spatial-temporal progression of the various critical boundary-layer flow points at selected oscillation frequencies and amplitudes, as well as the formation and convection of the LEV and the mechanisms responsible for the dynamic stall. The surface pressure data were integrated numerically to compute the variation in the unsteady lift and pressure drag forces and pitching moments. Flow visualization was used to aid the description of the viscous–inviscid interaction (e.g. LEV origin, strength, growth and development, and its shedding and convection over the airfoil upper surface). Three major oscillation cases, corresponding to the airfoil oscillated within (i.e. the attached-flow case) and through (i.e. the light-stall case), and well beyond (i.e. the deep-stall case) the static-stall angle, were studied. It is anticipated that these measurements will deepen our knowledge of unsteady boundary-layer separation and dynamic stall phenomena over an oscillating airfoil and their control.

2. Experimental apparatus and procedures

2.1. *Flow facility and test model*

The experiment was performed in the $0.9\,\mathrm{m} \times 1.2\,\mathrm{m} \times 2.7\,\mathrm{m}$ low-speed, suction-type wind tunnel in the Aerodynamics Laboratory at McGill University with a free-stream turbulence intensity of 0.08% at a free-stream velocity $u_\infty = 35\,\mathrm{m\,s^{-1}}$. An NACA 0012 airfoil, fabricated from solid aluminium, with a chord length, c, of 15 cm and a span of 37.5 cm was used as the test model. The origin of the coordinate was located at the leading edge of the airfoil with x, y and z in the streamwise, normal and spanwise directions, respectively. The airfoil was fitted with two 30 cm-diameter endplates with sharp leading edges to isolate the end effects. The gaps between the oscillating airfoil and the stationary endplates were kept at less than 1 mm to minimize the leakage of flow through the gaps. This two-dimensional configuration approximated an airfoil with an effective aspect ratio of infinity (Lee & Birch 2004). The two-dimensional uniformity of the flow distribution over the airfoil model was checked by traversing a 5 μm hot-wire probe located at 10% of c downstream from the leading edge of the airfoil and $y = 5\,\mathrm{mm}$ above the airfoil. The non-uniformity was found to be $\pm 4\%$ of the free-stream value. A specially designed four-bar-linkage and flywheel oscillation mechanism, capable of oscillating the airfoil sinusoidally at various amplitudes and frequencies, was used in the present experiment. The mean angle of attack, α_m, was varied by changing the rotating shaft at specific radial shaft-connector locations. The oscillation amplitude, $\Delta\alpha$, was varied by attaching the rod at specific radial locations on the flywheel. A range of oscillation frequencies, $f_0 = 0.05$ to 8.5 Hz, were obtained using a timing belt and pulley system attached to a variable-speed d.c. motor. The oscillation frequency was measured to an accuracy of ± 0.02 Hz. The airfoil pitch axis was located at 1/4-chord. The instantaneous angle of attack, $\alpha(t)$ $(= \alpha_m + \Delta\alpha \sin \omega t$,

where $\omega = 2\pi f_0$ is the circular frequency and t is the time), of the airfoil and the phase reference signal, $\tau = \omega t$, were recorded by using a potentiometer (TRW type DP 801) with an accuracy of $\pm 0.1°$. The airfoil was oscillated both within, through, and well beyond the static-stall angle, α_{ss}, with a reduced frequency, $\kappa = \omega c/2u_\infty$, ranging between 0.0125 and 0.3 at a chord Reynolds number, Re ($= u_\infty c/\nu$, where ν is the fluid viscosity), of 1.35×10^5. Note that when the phase angle is within the range $0 \leqslant \tau \leqslant 0.5\pi$ (or $0 \leqslant \tau \leqslant 90°$) and $1.5\pi \leqslant \tau \leqslant 2\pi$ (or $270° \leqslant \tau \leqslant 360°$), the airfoil is described to be in pitchup or upstroke; when $0.5\pi \leqslant \tau \leqslant 1.5\pi$ (or $90° \leqslant \tau \leqslant 270°$), the airfoil is said to be in pitchdown or downstroke. Also, in the following discussion, the suffix u is used to indicate pitchup when the angle of attack is increasing and d is used to indicate pitchdown when the angle of attack is decreasing.

The wake of the airfoil model was examined by using a miniature hot-wire probe (DISA P11) with a Dantec 56C17 constant-temperature anemometer (CTA). The overheat ratio was set at 1.6. The hot-wire probe was mounted on a sting extended from a computer-controlled three-dimensional traversing mechanism, and was located at one chord downstream of the trailing edge of the airfoil. The probe was moved with accuracy in the y-direction of 20 μm. All hot-wire calibrations, mean-flow measurements, free-stream turbulence levels, r.m.s.-disturbances measurements, and the subsequent processing were performed on a Pentium III PC with a 16 bit A/D converter board. The hot-wire signals were sampled at 2 kHz. The instantaneous wake velocities were subsequently ensemble-averaged over a large number of oscillation cycles (ranging from 100 to 150) to obtain the phase-locked average of the mean and fluctuating velocity fields at various phase positions during the oscillation cycle.

The surface pressure distributions were obtained from 61 pressure taps (of 0.35 mm in diameter), in conjunction with seven fast-response miniature pressure transducers (Type YQCH-250-1), distributed over the upper and lower surfaces of the model. The orifices were staggered 1.5 mm apart in the streamwise direction to avoid the wake effect from an upstream orifice on orifices further downstream. The pressure signals were phase-averaged over 100 cycles of oscillation and were integrated numerically to compute the unsteady aerodynamic loads and pitching moments. The dynamic range of the pressure transducer was of the order of 10 kHz. The transducer signals were low-pass filtered (250 Hz) and amplified with a multi-channel AA Lab model G3006 pressure measurement system. The effects of the 18 cm long and 0.75 mm i.d. Tygon tubing, separating the surface tap and the pressure transducer, on the unsteady pressure signals were examined by comparing the transducer output level and the phase with a controlled acoustic sound source. Details of this method can be found in the work of Chen & Ho (1988) and Lee & Basu (1997). The effect of the length of the Tygon tubing was a simple time constant delay on all pressure signals with frequency above 2.95 Hz, which rendered a limited reduced frequency κ of 0.0993 at $u_\infty = 14\,\mathrm{m\,s^{-1}}$ or $Re = 1.35 \times 10^5$ in the present experiment. Therefore, as a result of the difficulties encountered with the inevitable lag in the transducer's response, the curves of lift and pressure drag coefficients, C_l and C_d, and the pitching-moment coefficient, C_m, for $\kappa > 0.1$ can only be considered qualitatively, but large hysteresis effects are apparent nevertheless. The overall flow structures around the static and oscillating airfoils were also visualized in a smoke tunnel, and were recorded with a 60 Hz video camera at a shutter speed of 1/1000 s. The video film was studied frame-by-frame to obtain qualitative measurements of the formation and movement of the leading-edge vortex and flow reversal, as well as the interaction between the boundary-layer flow and the free stream.

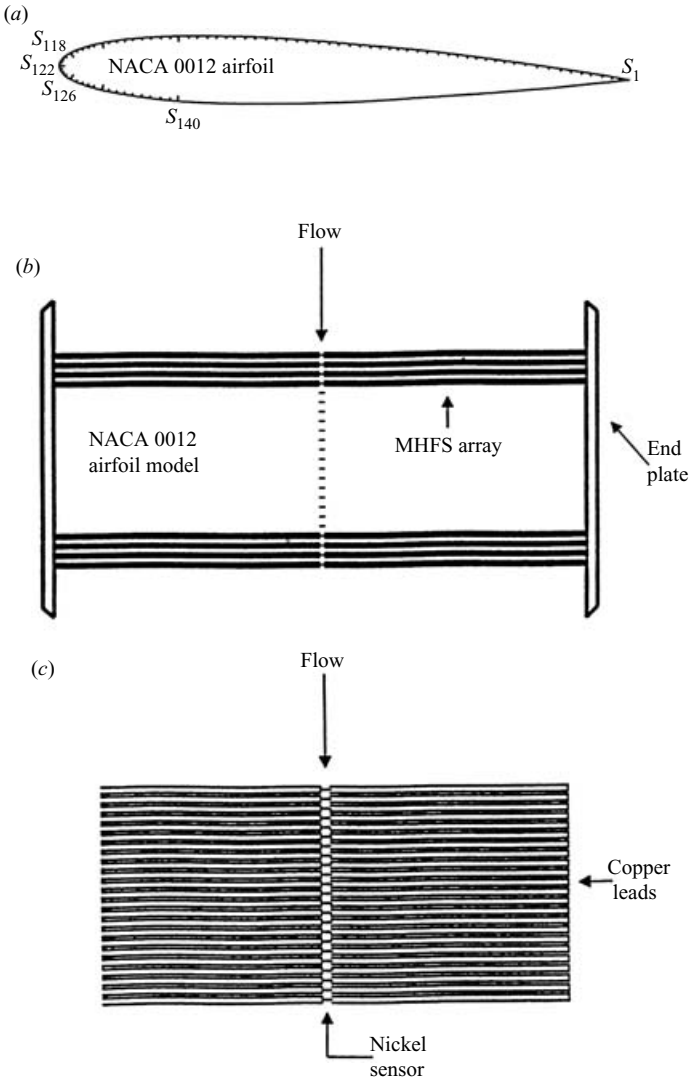

FIGURE 1. Schematics of (*a*) the NACA 0012 airfoil model and (*b*, *c*) MHFS arrays.

2.2. *Multi-element hot-film sensor (MHFS) array*

A total of 140 closely spaced multi-element hot-film sensors, which were electron-beam evaporated onto a thin polyimide substrate (50 μm thick), with a sensor spacing, *s*, of 1.25 mm arranged in a straight-line array, were used to identify the various boundary-layer and stall events both non-intrusively and simultaneously. Each sensor consisted of a nickel film 2 μm thick, 0.1 mm wide and 2 mm long with 10 μm copper-coated nickel leads routed to provide wire attachment away from the measurement location (figure 1*a*). The leads from the sensors were laid out along the span such that they were taken out through the end plates and the tunnel wall with practically no disturbance to the flow. The nominal resistance of the sensor was 8 Ω. Sensors S_1–S_{121} and S_{123}–S_{140} were on the upper and lower surfaces of the airfoil, respectively, with sensor S_{122} located at the leading-edge stagnation point (LESP) for $\alpha = 0°$. The sensor number indicates the location of the hot-film sensors along the surface of the airfoil,

and is proportional to the distance covered along the lower and upper surface of the airfoil from the LESP. The entire sensor array was bonded onto the airfoil model using double-sided Mylar adhesive tape (50 μm in thickness), which prevented the sensor array from introducing surface irregularities to the model surface. The sensor pattern and layout of the copper leads are shown in figure 1(*b*, *c*).

Groups of 15 of the 140 hot-film sensors were systematically connected to 15 AA Lab model AN-2000 constant-temperature anemometers (CTAs) to obtain the time history of the heat transfer output or wall shear stress at each sensor position. The sensors were connected to the CTAs by using a magnet wire and BNC coaxial cable combination to minimize the disturbance to the flow in the tunnel test section. The overheat ratio was set at 1.09 which ensured that only a small amount of heat was introduced, and that the heated thin films caused little disturbance to the shear layer or to each other. This was checked by heating the films individually and in groups while monitoring the effects on other films. The overheat ratio and d.c. offset voltage for each hot-film sensor were carefully adjusted such that each sensor was at nearly the same operating conditions. The CTA output signals were low-pass filtered and amplified by a gain between 10 and 50, and were sampled and digitized at 2 kHz per channel. The output signals from the potentiometer were also sampled and served as reference signals between each set of CTA output signals. The amplified signals were also connected to a four-channel oscilloscope (LeCroy model 9304) to provide on-line time history traces of the operating group of sensors. Details of the hot-film sensor arrays and their operation are given in Lee & Basu (1998) and Lee (1999).

No calibration of the MHFS was performed on the CTA system as the objective of the present experiment was to document the qualitative behaviour of the boundary-layer shear stress characteristics developed on the airfoil surface. The qualitative and direct extraction of the state of the boundary layer greatly relieves the difficulties encountered in the calibrating of multiple hot-film wall-shear stress sensors (Lober *et al.* 1992; Desgeorge & Lee 2002). Furthermore, although the response of a single hot film never becomes negative, a minimum is reached as the flow direction in the boundary layer changes sign, and this characteristic can be used to infer flow reversal. Similarly, the laminar–turbulent transition and its return to laminar flow developed on an unsteady airfoil are indicated by a rapid rise and fall in the heat transfer output levels. It is significant to note that the output of the hot-film sensors proved to be the most sensitive and definitive indicator of flow reversal and separation, and transition and reattachment, as well as the shedding and convection of the passage of the leading-edge vortex; it, therefore, served conveniently as the primary diagnostic tool for determining the various unsteady boundary-layer events and stalling mechanisms.

3. Results and discussion

3.1. *Static airfoil*

To facilitate the investigation of the unsteady boundary layer and stall events that occurred on an oscillating airfoil, the critical boundary-layer flow points (such as the leading-edge laminar separation and transition, and the trailing-edge turbulent flow separation points) that occurred on a static NACA 0012 airfoil were characterized first and serve as a frame of reference for dynamic stall results. Figure 2(*a*) shows the rear-to-front progression of these critical flow points with increasing airfoil incidence at $Re = 1.35 \times 10^5$. Similar to the linear lift-curve slope, $C_{l\alpha} = \mathrm{d}C_l/\mathrm{d}\alpha = 0.08$, presented for $\alpha < 10^\circ$ before the pre-stall loss of lift (figure 2*b*), the locations of the laminar separation and transition, and the trailing-edge turbulent flow separation points also

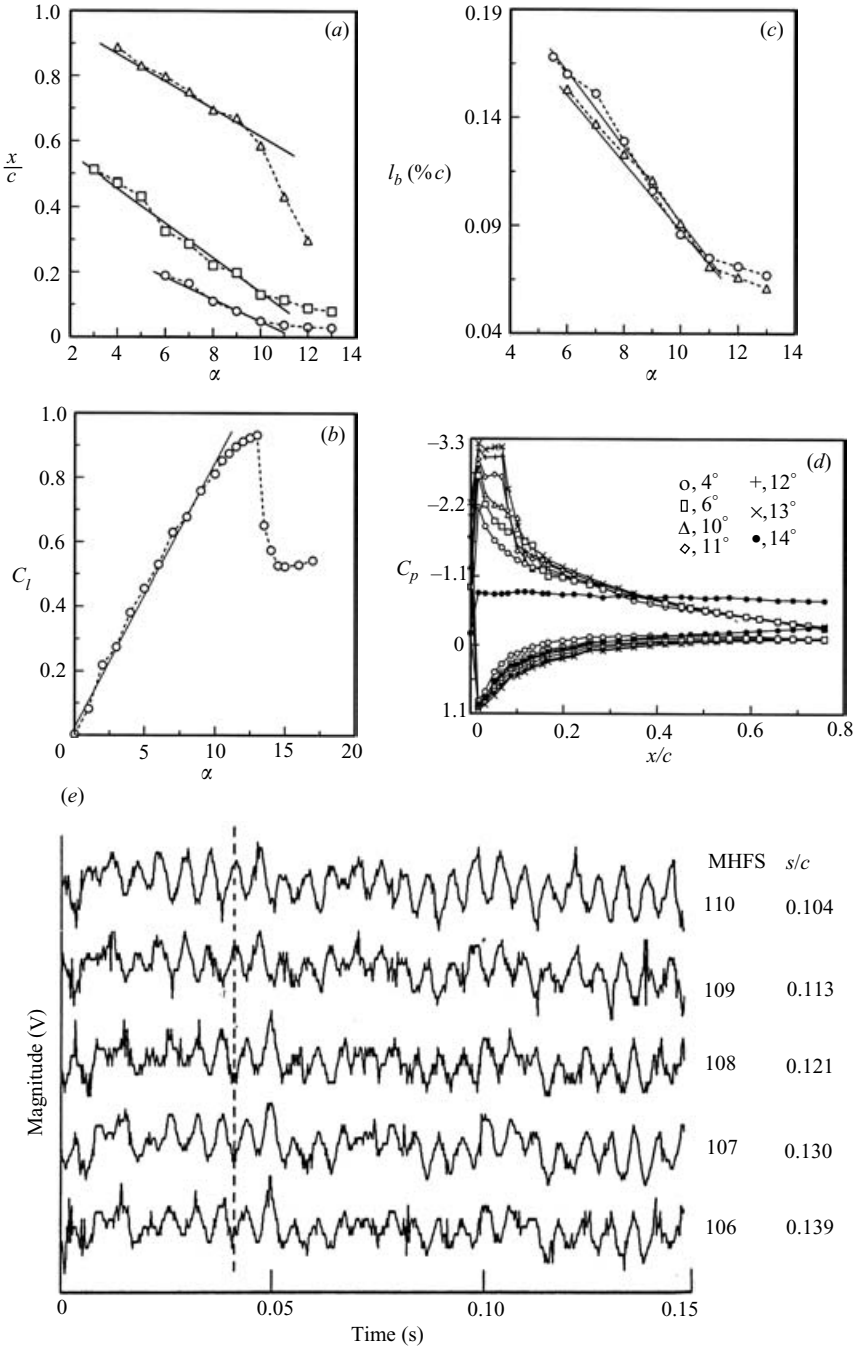

FIGURE 2(*a–e*). For caption see facing page.

moved upward in a linear manner toward the leading edge for $\alpha < 10°$, but at different rates or slopes; a slope, $\mathrm{d}(s/c)/\mathrm{d}\alpha$, of 0.03125, 0.117 and 0.047 was approximated for the laminar separation and transition, and trailing-edge flow separation points, respectively. For $\alpha > 10°$, the critical flow points and the lift coefficient spread upstream

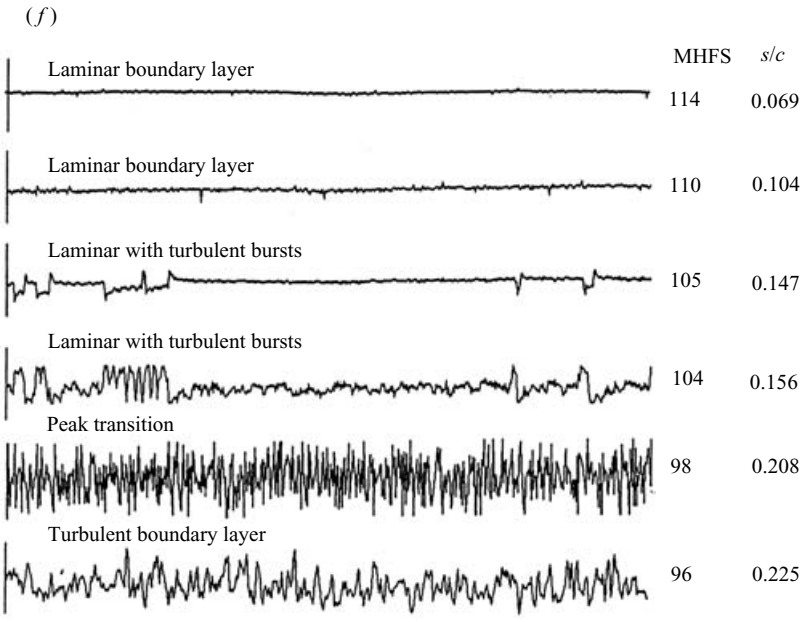

FIGURE 2. Boundary-layer events of a static NACA 0012 airfoil at $Re = 1.35 \times 10^5$. (*a*) critical flow points: ○, laminar separation; □, peak transition, △ trailing-edge flow separation, (*b*) C_l–α curve, (*c*) bubble length l_b, ○, C_p; △, MHFS, (*d*) C_p distributions, and MHFS identification of (*e*) laminar separation and (*f*) boundary-layer transition.

or increased with α both rapidly and nonlinearly. The identification of the laminar separation and transition are discussed in figures 2(*e*) and 2(*f*). The shortening of the laminar separation bubble and its movement to the leading edge with increasing α can be clearly seen in figure 2(*c*). The existence of a laminar separation bubble was also confirmed from the plateaux in the surface pressure distributions (up to $\alpha = 13^\circ$) in the leading-edge region of the airfoil (figure 2*d*). For $\alpha > 13^\circ$, the boundary layer completely separated from the leading edge and rendered a flat surface pressure distribution. It is therefore concluded that for a static NACA 0012 airfoil at $Re = 1.35 \times 10^5$, the stalling mechanism is of a sharp leading-edge stall type and was precipitated by bubble bursting. A static stall angle, α_{ss}, of 13° was observed.

Figure 2(*e*) illustrates the non-intrusive identification of the laminar separation point based on the 180° out-of-phase phenomenon observed across sensors of interest in the leading-edge region. The numbers shown on the right-hand side ordinate axis correspond to sensor numbers as well as the distance s/c from the leading edge of the airfoil. The left-hand side ordinate axis indicates the self-scaled hot-film output voltage level. An 180° phase shift between the outputs of S_{108} and S_{109}, indicating the location of the laminar separation point at $s/c \approx 0.113$, is evident. The turbulent separation point could not be detected owing to the random wide-band frequency content of turbulent surface shear-stress signals, and, therefore, was estimated from the flow-visualization results. Figure 2(*f*) shows the normalized hot-film outputs had low voltage amplitudes if the boundary layer was laminar. As the boundary layer became unstable, periodic turbulent bursts began to appear with associated increase in the hot-film output amplitudes. The amplitude, or the r.m.s. value, reached a maximum at peak transition. It was followed by a slight decrease in the amplitude or r.m.s. level in the turbulent region. The onset and end of transition was found to

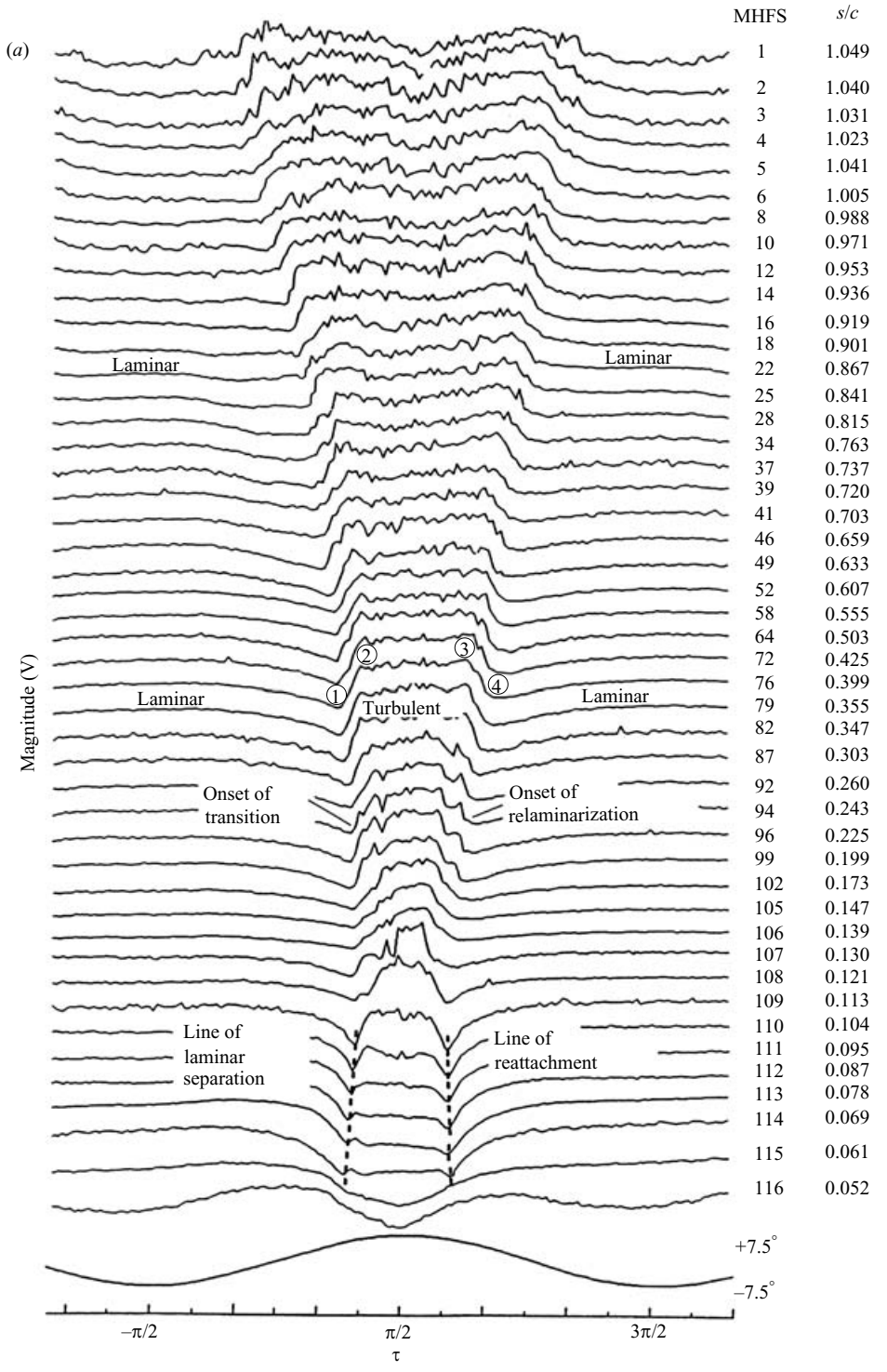

FIGURE 3(*a*). For caption see facing page.

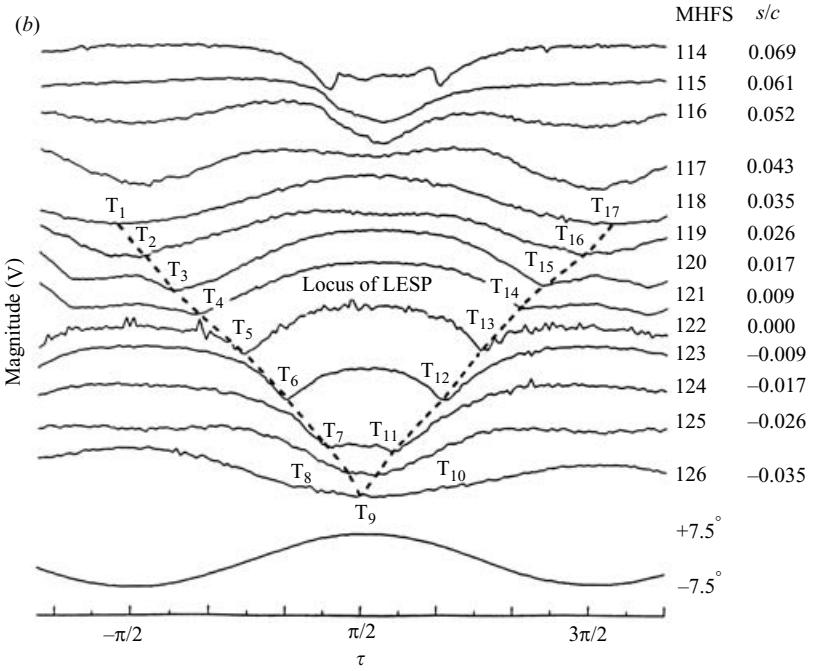

FIGURE 3. Representative MHFS signals for $\alpha(t) = 0° + 7.5°\sin\omega t$ at $\kappa = 0.05$. (*a*) S_1–S_{116} and (*b*) S_{114}–S_{126}. T_1–T_{17} denote the locus of LESP. Points ①–② denote transition, ②–③ attached turbulent boundary layer, and ③–④ the return to the laminar state.

generally cover about 4–5% chord length. For an unsteady airfoil, the interpretation of the hot-film signals is, however, more straightforward because the changes from one flow state to another can be more readily identified than in the steady-state-flow case.

3.2. *Oscillating airfoil*

3.2.1. *Airfoil oscillated within* α_{ss}

Figure 3 presents the representative MHFS signals from an NACA 0012 airfoil oscillated at $\kappa = 0.05$ with $\alpha(t) = 0° + 7.5° \sin\omega t$. The lowest curve represents the variation in the potentiometer voltage and phase information. The transition and its return to the laminar flow state were apparent as α increased and then decreased, and were identified directly by a rapid increase and drop in the hot-film heat transfer levels. The delay of the upward transition, relative to the static case, and the promotion of the rearward relaminarization points were found to behave in a nonlinear manner (figure 4*a*, *b*). The hot-film measurements also indicate that, for an airfoil oscillated with the maximum angle of attack $\alpha_{max} < \alpha_{ss}$, (i) the flow remained mainly attached throughout the cycle (except in the region close to the trailing edge where flow separation always persisted) and the behaviour of the airfoil can be approximated by the classical linear inviscid theory; (ii) there existed a wake vortex pattern, similar to the characteristics of the natural von Kármán vortex shedding, indicating that the boundary layer on the airfoil was laminar at low airfoil incidence; (iii) the laminar separation bubble (as indicated by the line of laminar separation between $s/c = 0.069$ and $s/c = 0.113$ was shortened and had a bubble length $l_b = 4.4\%$ of c, compared to a static value of $l_b = 11\%$ of c, at $\alpha = 7.5°$; (iv) similar to the case of a static

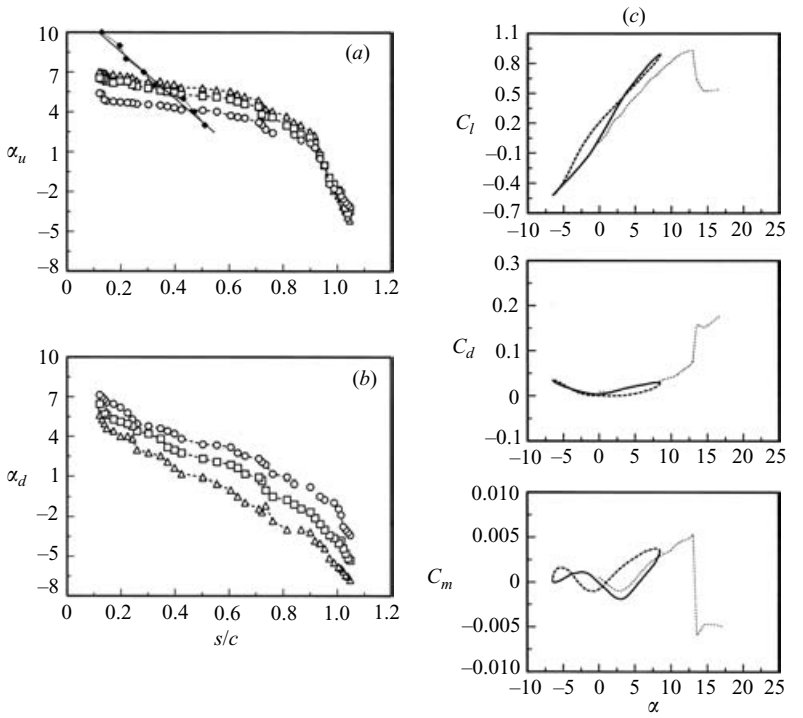

FIGURE 4. Loci of boundary-layer (*a*) transition and (*b*) relaminarization for $\alpha(t) = 0° + 7.5° \sin \omega t$: ○, $\kappa = 0.025$; □, 0.05; △, 0.1. (*c*) dynamic-load loops for $\kappa = 0.05$: ——, increasing α; ···, decreasing α; · · ·, static values. ◆, static airfoil.

airfoil, the turbulence followed laminar separation and a bubble occurred during the upper part at high incidence; (v) there existed a small hysteresis, or asymmetry, in the transition–relaminarization cycle; (vi) the attached-flow lift coefficient C_l-α curve led the static lift and had an increase in the lift-curve slope $C_{l\alpha}$ (figure 4*c*), but was accompanied by an increased C_m, compared to those of a static airfoil; and (vii) the hysteresis loops were narrow and the C_d values forming them did not deviate significantly from the statically obtained values.

Figure 4 also indicates that for an airfoil oscillated with $\alpha_{max} < \alpha_{ss}$, the primary influence of the reduced frequency was to delay the forward motion of the transition point, and to allow the turbulent boundary layer to withstand the imposed retardation, without suffering flow reversal, at substantially higher α than would be possible under static conditions. As κ increased, the onset of transition and its return to the laminar state were further delayed and promoted, respectively, and with a lesser degree of asymmetry, or hysteresis, in the transition–relaminarization cycle. The laminar bubble was found to remain quiescent and its length insensitive to the reduced frequency.

The nature of the attached boundary-layer flow at different phases, or instantaneous angles of attack, can also be illustrated from the three-dimensional composite plots of the variation of the phase-locked ensemble-averaged mean velocity and turbulence intensity profiles of the airfoil wake (figure 5*a*). The sinusoidal hill of the velocity deficit, resulting from the periodic movement of the trailing edge, also induced high-intensity double peaks. Figure 5(*a*) clearly indicates that for an airfoil oscillated with $\alpha_{max} = 7.5°$, the wake thickness and deficit and also the turbulence intensity were much smaller than those of a static airfoil (figure 5*b*). In summary, for an airfoil oscillated

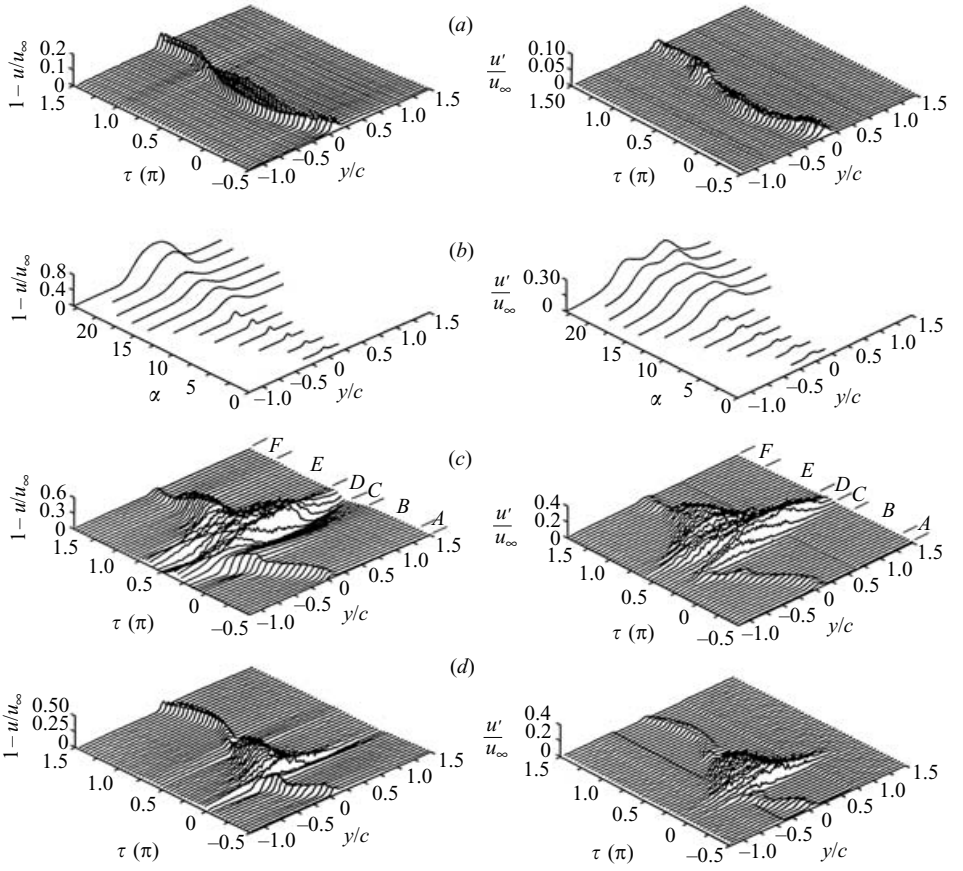

FIGURE 5(*a–d*). For caption see next page.

with $\alpha_{max} < \alpha_{ss}$, the various boundary-layer events were delayed nonlinearly relative to the static case when the incidence is increasing; i.e. they occurred farther from the leading edge for a given value of α, or at larger incidence for a given s/c. Conversely, the same events occurred sooner when α was decreasing. The attached-flow oscillation case also rendered an increased lift-curve slope and lift coefficient and positive values of C_m, but the pressure drag coefficient remained basically the same compared to the static values. Finally, note that the MHFS measurement of the instantaneous location of the LESP, identified by the locus of the travel of the point of minimum MHFS voltages (denoted by the dashed lines in figure 3*b*) in the leading-edge region of the airfoil, also provides an alternative means for the determination of the wing instantaneous angle of attack, and a wing-stall warning indication.

3.2.2. *Airfoil oscillated beyond* α_{ss}

For an airfoil oscillated well beyond the static-stall angle, the unsteady boundary layer and stall events became more complicated owing to the presence and the upward spread of the flow reversal and turbulent breakdown, and the subsequent growth and convection of an energetic leading-edge vortex (LEV), in addition to the accompanied large hysteresis in the dynamic load loops. Figure 6 shows the representative MHFS signals at $\kappa = 0.1$ with $\alpha(t) = 10^\circ + 15^\circ \sin \omega t$; i.e. with $\alpha_{max} = 25^\circ$. Similar to the attached-flow case shown in figure 3, the boundary-layer transition to turbulence

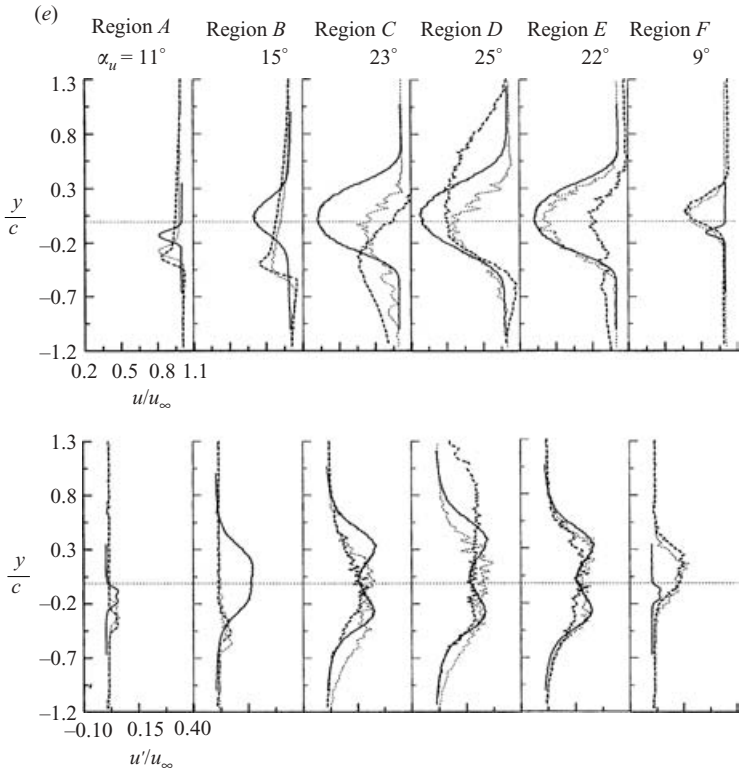

FIGURE 5. Three-dimensional representation of the phase-locked ensemble-averaged wake mean and fluctuating velocity profiles. (*a*) $\alpha(t) = 0 + 7.5° \sin \omega t$ and $\kappa = 0.05$, (*b*) static airfoil, (*c*) $\alpha(t) = 10° + 15° \sin \omega t$ and $\kappa = 0.1$, and (*d*) $\alpha(t) = 0° + 15° \sin \omega t$ and $\kappa = 0.05$. (*e*) Two-dimensional presentation of (*c*) at selected $\alpha(t)$ corresponding to regions *A*–*F* with $\cdots$, $\kappa = 0.05$; $\bullet\bullet\bullet$, $\kappa = 0.1$; —, static airfoil.

and its return to the laminar-flow state can be clearly identified from the sharp rise and fall of the hot-film output levels during each cycle of oscillation. The flow remained attached, except in the trailing-edge region, for angles of attack up to about $\alpha_{ss} = 13°$. However, in contrast to the rear-to-front progression of the trailing-edge flow separation with increasing α occurring on a static airfoil, a flow reversal, characterized by a thin layer at the bottom of the thickened turbulent boundary layer (see also figures 7*a*, *h*), was observed for an airfoil oscillated beyond α_{ss}. The flow reversal was first observed at $\alpha_u = 12.9°$ (or $s/c = 0.884$) and propagated gradually upstream up to $s \approx 26\%$ of c (about the 1/4-chord pitch location) at $\alpha_u = 21.6°$. Upstream of the flow reversal the boundary layer remained attached to the airfoil between $s/c \approx 0.138$ and 0.26 and was preceded with a shortened laminar separation bubble (existing between $s/c \approx 0.034$ and 0.095 and with a bubble length l_b of 6.1% of c). At $\alpha_u = 21.8°$, the attached turbulent boundary layer underwent a sudden breakdown at $s/c \approx 0.14$. The flow reversal and the turbulent breakdown were identified based on the local minimum in the sensor S_{20}–S_{92} outputs (covering $s/c = 0.26$ to 0.884) and from the monotonic decrease in the sensor S_{106} at $s/c = 0.14$, denoted by Δ symbols and $\downarrow$ signs, respectively. Note that near the trailing edge (S_{18}–S_2; $s/c > 0.901$), the trailing-edge flow reversal was intermittent and could not be ascertained in the presence of random turbulent fluctuations. As the airfoil continued to pitch up, the turbulent breakdown

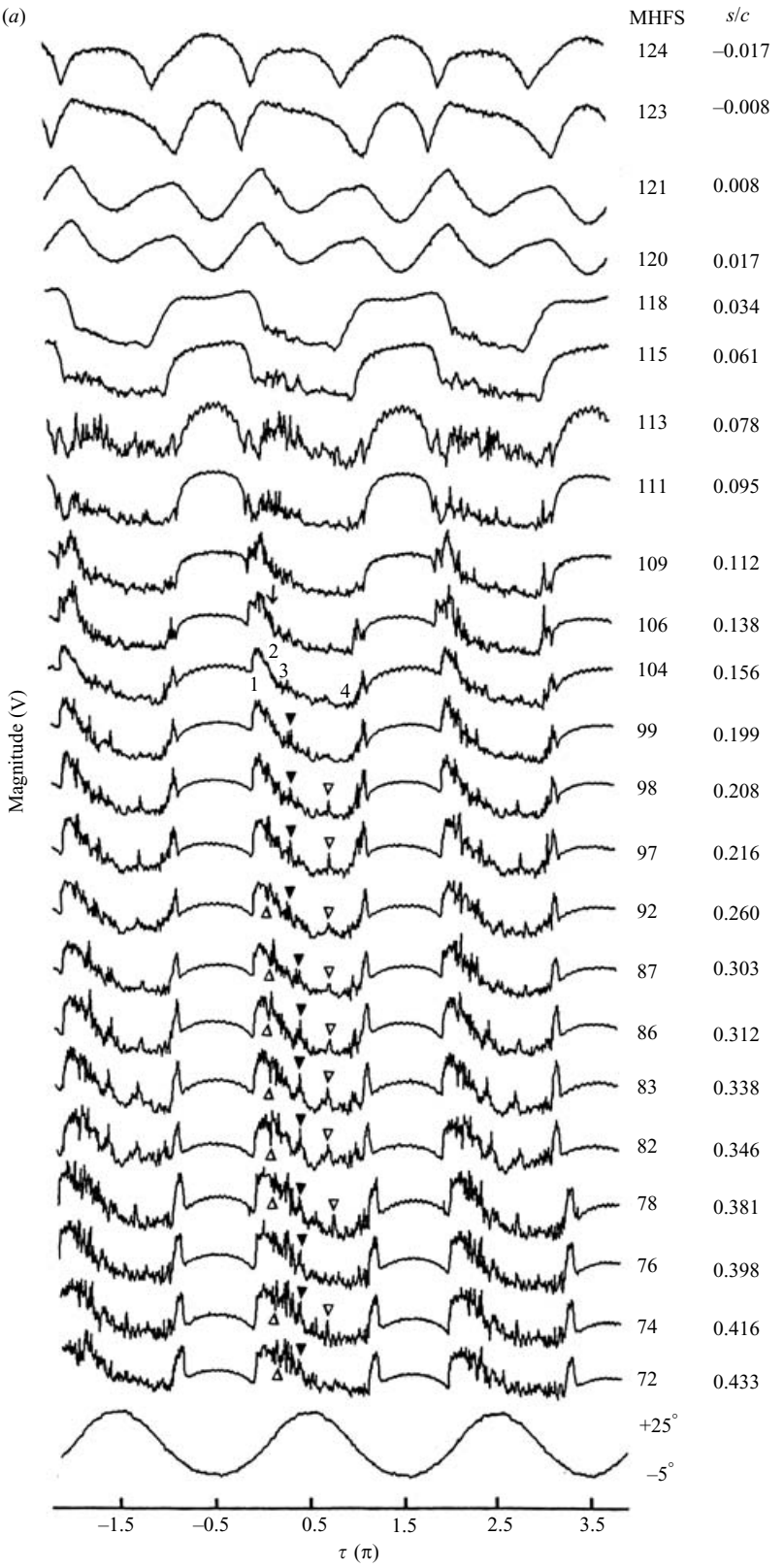

FIGURE 6(*a*). For caption see next page.

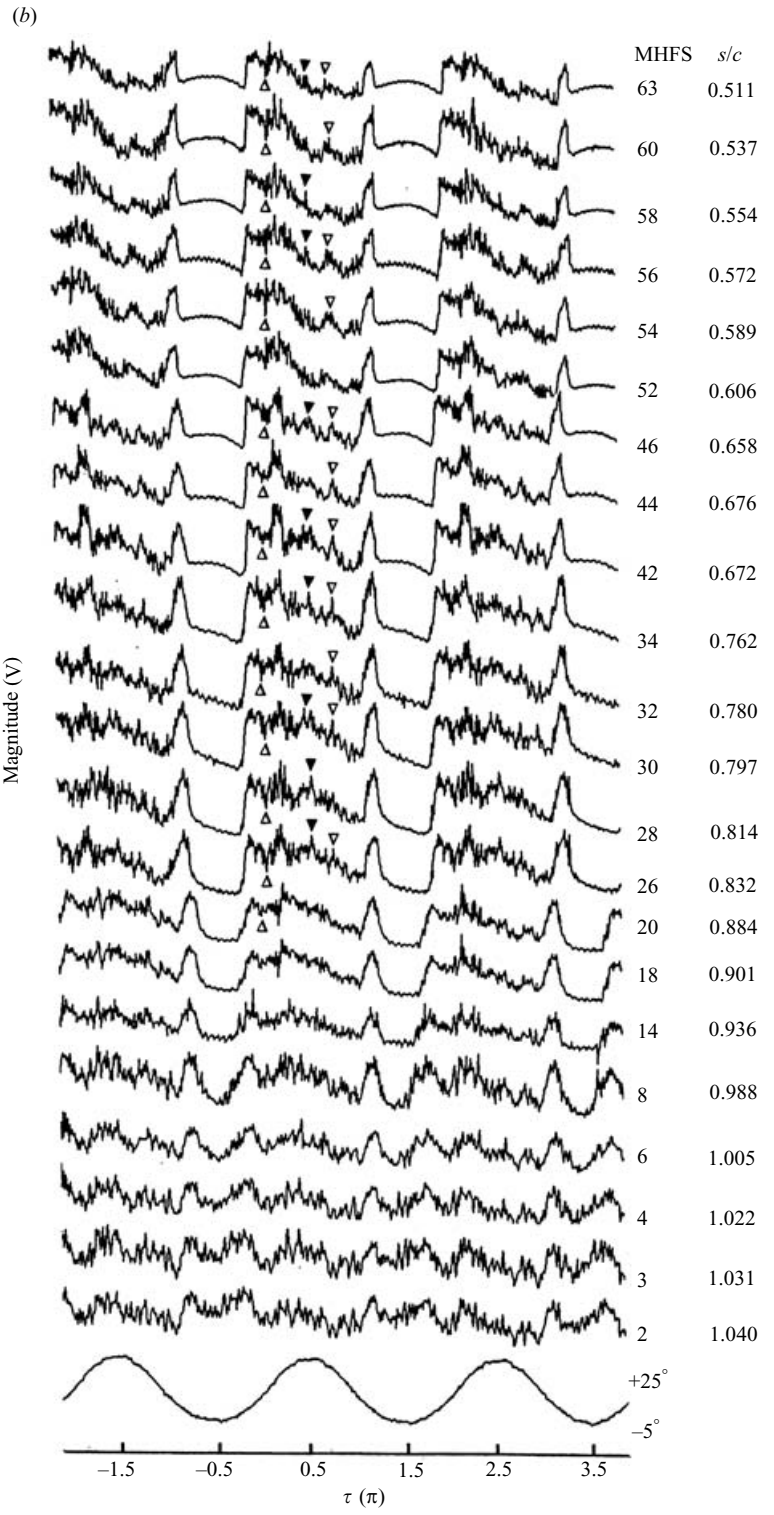

FIGURE 6. Representative MHFS signals for $\alpha(t) = 10° + 15°\sin\omega t$ with $\kappa = 0.1$. (*a*) S_{124}–S_{72} and (*b*) S_{63}–S_2. △, flow reversal; ↓, turbulent separation; ▼, passage of LEV; and ▽, passage of secondary vortex. ①, onset of transition; ②–③ turbulent breakdown; ③–④, separated flow.

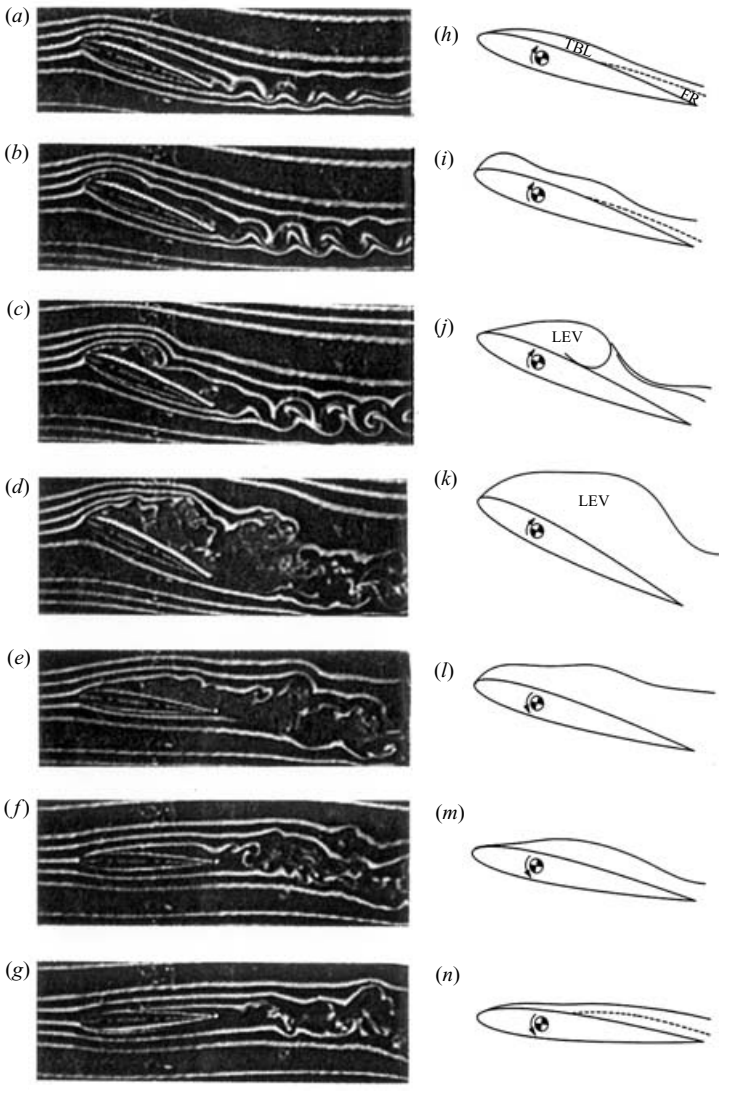

FIGURE 7. Selected sequences of boundary-layer events both prior to, during, and after stall at $\kappa = 0.1$ for $\alpha(t) = 10^\circ + 15^\circ \sin \omega t$: (*a*) upward spread of flow reversal for $12.9^\circ < \alpha_u < 21.6^\circ$; (*b*) turbulent breakdown and the formation of LEV at $\alpha_u = 21.9^\circ$; (*c*) LEV growth and rearward convection for $\alpha_u = 22.4^\circ$–24.4°; (*d*) LEV catastrophic detachment at $\alpha_u = 24.7^\circ$; (*e*) separated flow for $\alpha_d > 14.1^\circ$; (*f*, *g*) rearward reattachment for $\alpha_d < 14.1^\circ$; (*h*)–(*n*) are the conceptual sketches of (*a*)–(*g*), respectively. TBL denotes turbulent boundary layer and FR denotes flow reversal.

moved rapidly both upstream and downstream, disrupting the laminar separation bubble, and initiated the formation of an LEV with an initial length of about 14% of c at $\alpha_u = 21.9^\circ$. The LEV grew and convected rapidly downstream (denoted by ▼ symbols) with a further increase in the airfoil incidence for $\alpha_u = 21.9^\circ$ to 24.4°. At $\alpha_u = 24.7^\circ$ (near the top of the airfoil pitchup motion), the LEV grew to about 90% of the chord length of the airfoil and rendered a maximum lift coefficient, C_{lmax}, of 2.44, compared to 0.92 for a static airfoil, and a dynamic stall or lift stall, L, at $\alpha_{ds} = 24.7^\circ$

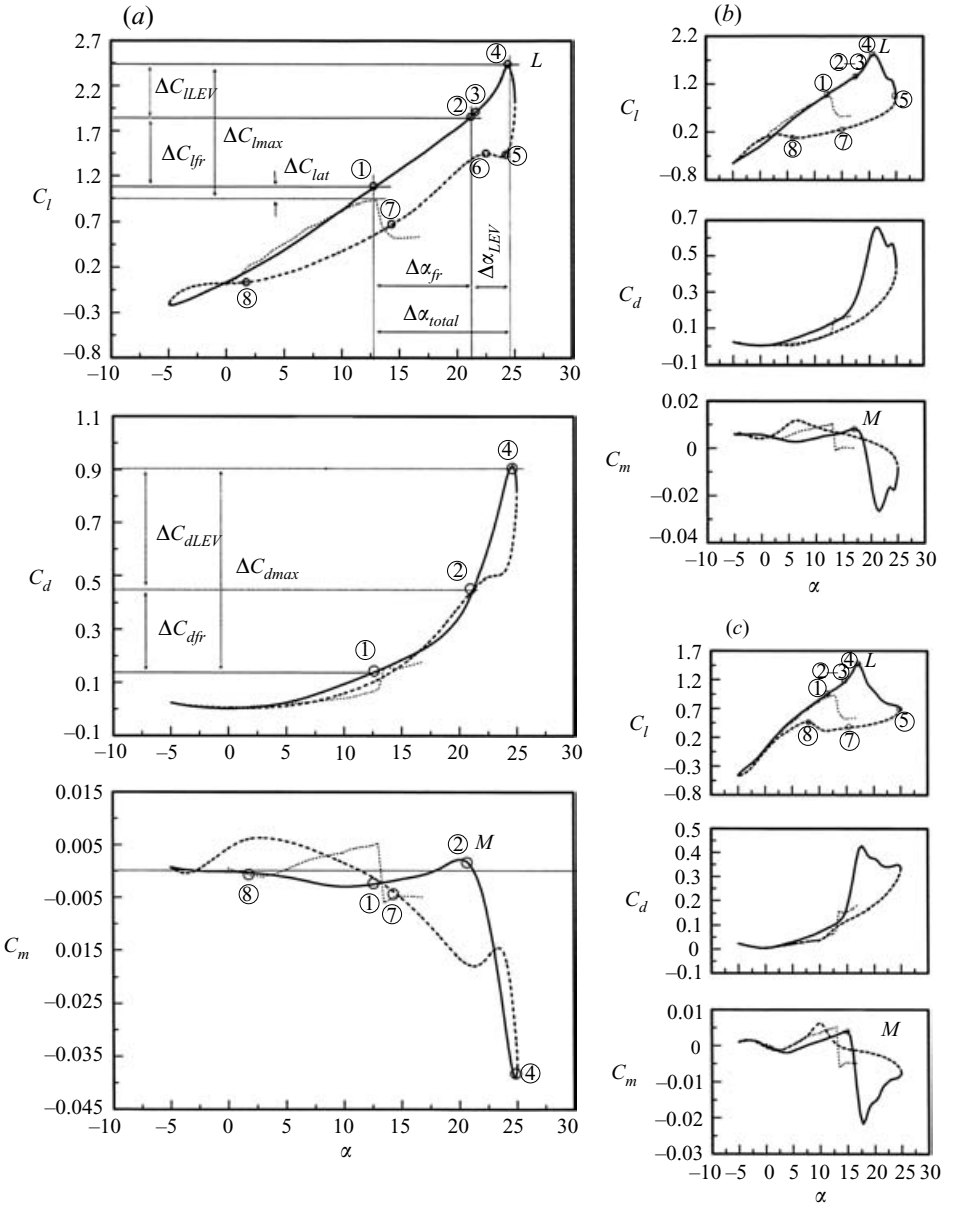

FIGURE 8. Variation of dynamic load-loops with reduced frequency for $\alpha(t) = 10° + 15°\sin\omega t$. (*a*) $\kappa = 0.1$, (*b*) $\kappa = 0.05$, (*c*) $\kappa = 0.025$. ①, onset of flow reversal; ②, end of upward spread of flow reversal; ③, turbulent breakdown; ④, lift stall; ④–⑤, full stall; ⑥, onset of secondary vortex; ⑦, onset of flow reattachment; ⑧, end of flow reattachment. ——, increasing α; ····, decreasing α; · · ·, static values; *M*, moment stall; *L*, lift stall.

(figure 8*a*). After the LEV reached and passed off the trailing edge, the airfoil became completely stalled for a brief period, and a somewhat weaker rearward convected secondary vortex (denoted by ∇ symbols) was observed to form at $\alpha_d = 21.8°$ during downstroke, rendering a slight increase in the lift coefficient (denoted by point ⑥ in figure 8*a*). After the secondary vortex passed off the trailing edge, the separated

boundary-layer flow began to reattach to the airfoil at $\alpha_d = 14.1^\circ$ and became fully attached at $\alpha_d = 1.1^\circ$ for the rest of the oscillation cycle. A qualitative depiction of the flow structure around the airfoil at selected $\alpha(t)$ is given in figure 7.

For $\alpha_{max} \gg \alpha_{ss}$, the most significant unsteady boundary-layer phenomena both prior to, during, and post the stall can be summarized as follows: prior to the dynamic stall, the flow remained attached up to about α_{ss}. For $\alpha_{ss} < \alpha_u < \alpha_{ds}$, the boundary-layer flow was characterized by the rear-to-front spread of the trailing-edge flow reversal (while not showing any strong variations in the boundary-layer thickness, or with little or no distortion of the external stream until the formation of an LEV) and a sudden turbulent breakdown, and the following formation and rearward convection of an energetic LEV, which is mainly responsible for the large variation in the C_l–C_d–C_m values compared to the static counterparts; a characteristic attributed to the transient effects (as suggested by Ericsson & Reding 1988), or to the apparent camber effects (as suggested by Jumper *et al.* 1989). During the stall, the flow remained fully separated and with the presence and rearward convection of a secondary vortex. The post-stall condition was characterized by the gradual front-to-rear reattachment of the separated flow to the airfoil surface, and the return to the unstalled flow values. The MHFS signals also lead us to conclude that the NACA 0012 airfoil did not stall because of bubble bursting (as opposed to the sharp leading-edge stall caused by the bubble bursting observed for a static NACA 0012 airfoil); instead the dynamic stall began with an abrupt turbulent separation a short distance downstream of the bubble reattachment point. The turbulent separation point then moved both upward and rearward rapidly with increasing angle of attack until it reached the bubble, causing the bursting of the laminar bubble. The bubble only served to cause transition to turbulence for $\alpha \geqslant 6.5^\circ$. These boundary-layer events also reflected from the wake flow measurements shown in figure 5(*c*). The spatial-temporal progression of the critical flow points and the loci of the LEV and the secondary vortex are summarized in figure 9.

Figure 5(*c*) presents the composite three-dimensional presentation of the phase-averaged streamwise mean and fluctuating velocity profiles during one cycle of oscillation for $\alpha(t) = 10^\circ + 15^\circ \sin \omega t$ with $\kappa = 0.1$. It is seen clearly that there is significant variation in the wake thickness and velocity deficit, as well as the turbulence levels at different stages of a deep-stall airfoil. The various boundary-layer events can be categorized into six regions (*A*–*F*). Regions *A* and *B* indicate the wakes corresponding to the flow regimes of attached flow and the onset and the end of the upward spreading of the flow reversal, and were characterized by narrower and more turbulent fields (compared to both those of a static airfoil or regions *C*, *D* and *E*). Region *C* corresponds to the rapid thickening and breakdown of the turbulent boundary layer and the subsequent formation and rapid front-to-rear convection of a leading-edge vortex. The corresponding wake flows were characterized by a large increase in both the mean and fluctuating velocity profiles and the wake thickness and deficit. Region *D* represents the massive separation, or full stall, conditions with a sharp increase in both the wake thickness and deficit and the turbulence intensity as well. In region *E*, the wake structures become much less rigorous representing the beginning and end of the flow reattachment process during downstroke. The wake flow characteristics returned to the unstalled values in region *F*. The variation of the wake thickness and deficit and the turbulence intensity at $\alpha_u = 11^\circ$, 15°, 23° and 25°, and $\alpha_d = 23^\circ$ and 9°, corresponding to the regions *A*–*F*, with reduced frequency can be seen more explicitly in figure 5(*e*). The values of these characteristics generally increased (or decreased) with reduced frequency for regions *C* and *D* (or region *E*),

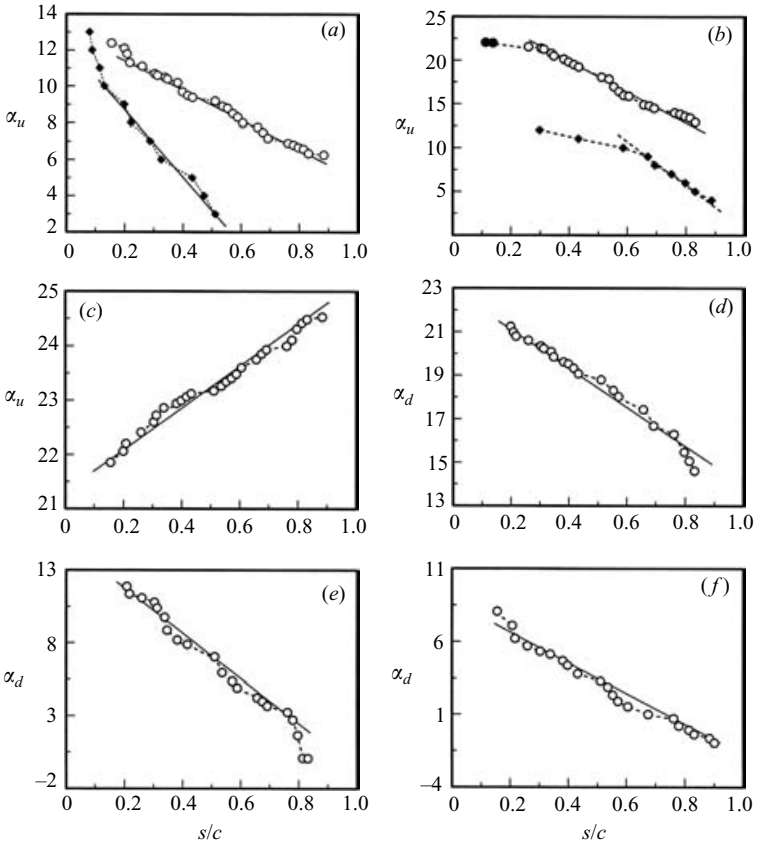

FIGURE 9. Loci of boundary-layer (*a*) transition, (*b*) flow reversal (○) and turbulent breakdown (●), (*c*) LEV, (*d*) secondary vortex, (*e*) reattachment, and (*f*) relaminarization for $\alpha\,(t) = 10^\circ + 15^\circ \sin \omega t$ at $\kappa = 0.1$. Note that only the clearly identifiable critical flow points were plotted. ◆, static airfoil.

while remaining comparable in regions *A*, *B* and *F*. Also shown in figure 5(*e*) are the static values. The thickening of the boundary layer, especially at the end of upward spread of the flow reversal, and the eruption into a violent wake (which appeared to have been substantially accomplished when the separation point caught up with the front of the reversed flow region) can also be seen from the two-dimensional representation of the wake flow structures.

Figure 9(*a*) shows that similar to the linear upward spread of the transition points of a static airfoil, the unsteady transition also moved upward gradually in a linear manner (between $s/c = 0.2$ and 0.9) for a deep-stall airfoil, but was delayed and at a lower rate ($\mathrm{d}(s/c)/\mathrm{d}\alpha = 0.145$) and at a propagation speed of about 40% of u_∞. Figure 9(*b*) shows that the flow reversal moved rather gradually and linearly upstream (at an approximate speed of 20% of u_∞ comparable to that of the trailing-edge flow separations of a static airfoil for $\alpha < 10^\circ$) up to an uppermost position of $s/c \approx 0.26$. The detection of the sudden turbulent breakdown could therefore serve as an indicator for dynamic stall and control. The loci of both the LEV and the secondary vortex (figures 9*c*, *d*) indicate that these vortices were travelling downstream at convection speeds $u_{LEV} \approx 0.45 u_\infty$ and $u_{2ND} \approx 0.30 u_\infty$, respectively. The reattachment line was found to proceed downstream at approximately 15% of the free-stream

velocity (figure 9*e*). There also existed a hysteresis between the onset of the boundary-layer transition and relaminarization (figure 9*f*) and between the unsteady separation and reattachment. Note that the observed hysteresis in the unsteady separation and reattachment may permit flutter to occur in a single degree of freedom of oscillatory body motion. With negative damping (figure 8*a*), the airfoil extracts energy from the flow, and the pitch oscillations will tend to increase in amplitude, unless restrained.

Moreover, by correlating the MHFS signals with the dynamic-load loops computed from the surface pressure measurements, the variations in C_l–C_d–C_m versus α curves, especially the stall angle delay and the lift increment, both before and during the stall could be quantified. Figure 8(*a*) shows that prior to stall, there was a slight increase in the lift coefficient $\Delta C_{lat} = 0.12$ (owing to the attached flow effect), but with the lift-curve slope $C_{l\alpha}$ remaining unchanged, compared to that of a static airfoil. The value of $C_{l\alpha}$ also remained roughly the same between points ① and ②, corresponding to the onset and end of the upward spread of the flow reversal for $\alpha_u = 12.9°$ to 21.6°, but with a large increase in the lift coefficient of $\Delta C_{l①–②} = \Delta C_{lfr} = 0.80$. ΔC_{lfr} denotes the lift coefficient increment due to the presence and upward movement of the flow reversal. A sharp rise in the values of C_l, $C_{l\alpha}$, C_d and $|C_m|$ was observed with the occurrence of the turbulent breakdown and the subsequent initiation, growth and convection of the LEV between points ③ and ④. A total increment in the dynamic lift coefficient of $\Delta C_{lamx} = C_{lat} + \Delta C_{lfr} + \Delta C_{lLEV} = 0.12 + 0.80 + 0.59 = 1.52$, compared to a maximum lift coefficient $C_{lmax,ss} = 0.92$ at α_{ss}, was achieved. The lift coefficient then underwent a sharp drop as soon as the LEV passed off the trailing edge, and the airfoil remained fully stalled (points ④–⑤). At point ⑥ ($\alpha_d = 21.8°$), there was a slight increase in C_l owing to the presence and convection of the secondary vortex. During post-stall, the drop in the lift and pressure drag coefficients persisted through the fully separated flow (points ⑥–⑦) until the completion of the reattachment (at point ⑧). Similarly, the C_d curve indicates that the drag did not begin its dramatic rise until the onset of the flow reversal (point ①); a ΔC_{dfr} increment of 0.31 was observed between the onset and end of the trailing-edge flow reversal. A further sharp rise in C_d was observed at the turbulent breakdown and the subsequent formation and spillage of the LEV (points ③–④). A maximum C_d ($= \Delta C_{dfr} + \Delta C_{dLEV} + C_{dmax,ss} = 0.31 + 0.45 + 0.0625$) of 0.8225 at $\alpha_{ds} = 24.7°$ (or the lift stall, L, at point ④) compared to a $C_{dmax,ss}$ of 0.0625 at α_{ss} was observed; a 13-fold increase in drag. The drag coefficient decreased sharply during the first stage of the post-stall condition (i.e. for the fully separated flow condition; $\alpha_u = 24.7°$ to $\alpha_d = 24.2°$) and returned to values comparable to the static counterparts starting at the onset of the flow reattachment (point ⑦). The moment stall, M, (corresponding to the angle of attack at which the pitching-moment coefficient started to decrease sharply, and was preceded by a gradual forward movement of flow reversal in a thin layer at the bottom of the turbulent boundary layer) occurred at the end of the upstream propagation of the flow reversal at $\alpha_u = 21.6°$ or point ②, and was a pitchdown moment. Peak negative pitching moment values occurred when the LEV reached 90% of the chord or at the lift stall angle. A peak value of $-C_m$ of 0.0395 at α_{ds}, compared to a $-C_m$ of 0.006 at α_{ss}, was observed; a 6.6-fold increase in C_m for a deep-stall NACA 0012 airfoil with $\alpha_{max} = 25°$ and $\kappa = 0.1$.

In summary, the airloads depend primarily on the time history of the angle of attack for the portion of the cycle where α exceeded the static-stall angle. The dominant effect resulting from the gradual forward movement of the flow reversal (at 40% of u_∞), and the formation and rapid rearward convection of the LEV (at 45% of u_∞) over the airfoil was to produce values of C_l, C_d and C_m that were far in excess of their

static counterparts. The dynamic vortex originated very close to the leading edge just prior to moment stall, M, and produced a large negative pitching moment, high drag and an additional increment in lift as it passed over the airfoil. However, note that for low-Reynolds-number flows (e.g. at $Re = 1.35 \times 10^5$), the presence and rear-to-front progression of the trailing-edge flow reversal contributed significantly to the increase in C_l and C_d, but not to any noticeable variation in $|C_m|$. Furthermore, although it appeared that the dynamics of the laminar separation bubble (of a shortened length of 6.7% of c) had a controlling influence on the events of dynamic stall, the bubble itself had little effect on the airfoil integrated loads, or even on the airfoil pressure distribution. The hysteresis observed in the dynamic-load loops originated from the asymmetry in the locations, or angles of attack, of the separation and the reattachment. Finally, although the boundary-layer flow reattached all the way to the trailing edge well before $\tau \approx 1.5\,\pi$, the aerodynamic loads did not return to their unstalled values until the airfoil passed through minimum incidence and started the next upstroke.

3.2.3. *Effect of reduced frequency*

The effects of reduced frequency on the unsteady boundary layer and dynamic-stall events, and the dynamic loads for $\alpha(t) = 10^\circ + 15^\circ \sin \omega t$ with $\kappa = 0.0125$ to 0.25 were also investigated and are summarized in figure 10. Figure 10(a) shows that for $\kappa < 0.2$, the approximated linear rear-to-front progression of the flow reversal persisted and was followed by an abrupt separation (denoted by solid symbols) over the front portion of the airfoil; these phenomena occurred at successively later times and increased rates as κ was increased. The onset and the uppermost location (i.e. to the vicinity of $s/c = 0.25$ for an NACA 0012 airfoil pitched at ¼-chord location) of the flow reversal were found to be insensitive to the reduced frequency. That is, the flow reversal was found to appear always at the rear portion of the airfoil and progress gradually up to $s/c = 0.26$, irrespective of the change in the reduced frequency, while the rate and the propagation speed at which the flow reversal travelled upstream were a strong function of the reduced frequency. Also, the turbulent breakdown was observed always at around 14% chord downstream from the leading edge, but at different upstroke angles of attack for different κ values. For $\kappa \geqslant 0.2$, the point of flow reversal spread upstream rapidly and in a rather nonlinear manner, and the turbulent separation did not take place until the instantaneous angle of attack reached its maximum value. At even higher κ, these events occurred almost simultaneously.

Figures 10(b) and 10(c) summarize the spatial-temporal movement of the LEV and the secondary vortex for $\kappa = 0.05$–0.2. The formation and rearward convection of the LEV was delayed to higher angles of attack as κ was increased. At low κ, the spillage or the catastrophic detachment of the energetic LEV occurred before the end of the upward pitching. At higher κ ($\geqslant 0.2$), this event was noticeably delayed and the LEV detachment occurred at the early stage of downstroke motion. However, once the LEV was formed, it seemed to convect over the airfoil at the same rate (i.e. with $u_{LEV} \approx 0.45 u_\infty$), implying that no special 'LEV-trapping advantage' was realized by changing κ values. The vortex-shedding phenomenon was not fundamentally different, but both its strength and its phase depended on κ. The increase in the lift-curve slope $C_{l\alpha}$ prior to stall was, however, more obvious with increasing κ (figure 8), and the continuous drop in C_l observed during the post-stall condition became much less significant with decreasing κ. Moreover, similar to the rearward convection speed of an LEV, the downstream convection speed of the secondary vortex, u_{2ND}, remained unchanged ($\approx 30\%$ of u_∞), and was insensitive to the reduced frequency. No secondary

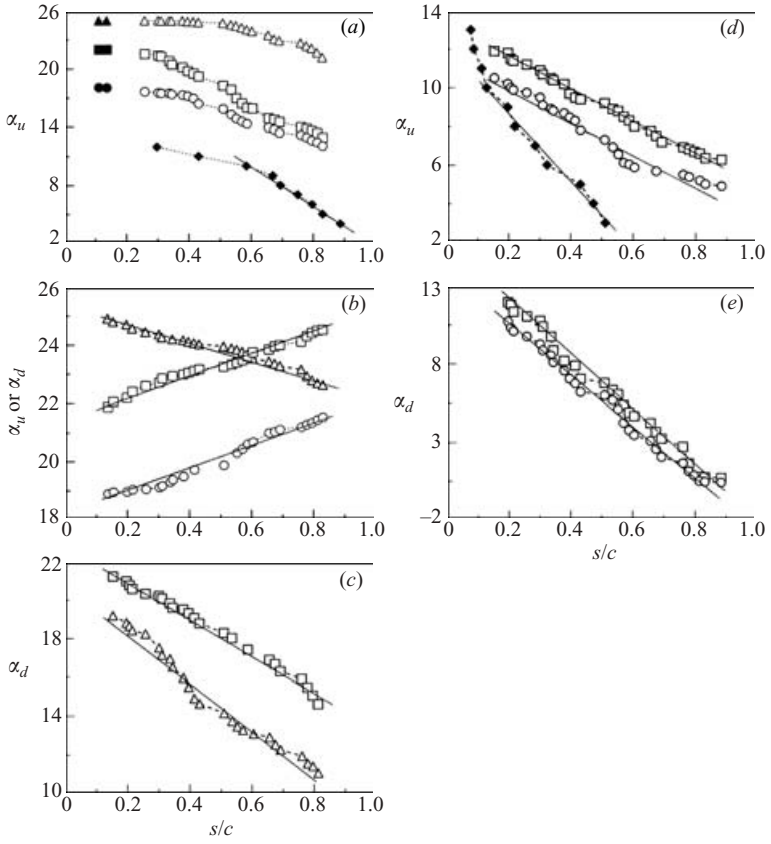

FIGURE 10. Effect of reduced frequency on boundary layer and stall events for $\alpha_m = 10°$ and $\Delta\alpha = 15°$: (*a*) flow reversal and separation; (*b*) LEV; (*c*) secondary vortex; (*d*) transition; and (*e*) reattachment. ○, $\kappa = 0.05$; □, 0.1; △, 0.2. Open symbols denote flow reversal and solid symbols turbulent breakdown. ◆, static airfoil.

vortex was, however, observed for κ less than 0.1. The variation of the stall angle delay ($\Delta\alpha_{fr}$ and $\Delta\alpha_{LEV}$), lift increment (ΔC_{lat}, ΔC_{lfr} and ΔC_{lLEV}), and α_{ds} with the reduced frequency is given in table 1. Table 1 shows that the reduced frequency not only caused a systematic delay in the onset of dynamic stall, but also determined whether the airfoil stalled well before α_{max}, or near the top of the oscillation cycle.

Figures 10(*d*) and 10(*e*) show that the trend in the delay (or promotion) of the upward (or rearward) transition (or reattachment) points along the airfoil upper surface always exhibited a linear manner, similar to that observed for a static airfoil for $\alpha < 10°$, but at a propagation rate insensitive to the reduced frequency. The phases, or the instantaneous angles of attack, at the onset and end of the boundary-layer transition and reattachment were, however, found to be a strong function of κ. Also, the laminar bubble length remained unchanged with increasing reduced frequency.

The effect of reduced frequency on the boundary-layer separation for an airfoil oscillating through α_{ss} with $\alpha_m = 0$ and $\Delta\alpha = 15°$ (i.e. a light-stall case) was also investigated (figure 11). In the light-stall oscillation case, the maximum angle of attack α_{max} was 2° above the static stall angle ($\alpha_{ss} = 13°$) and yet the airfoil did not stall owing to the 'LEV spillage'. The light-stall case is also of special significance to performance prediction, as it influences the values of various parameters (e.g. advance

https://doi.org/10.1017/S0022112004009851 Published online by Cambridge University Press

Oscillating case	κ	$C_{l,max}$	$\Delta C_{l,max}$	ΔC_{lat}	ΔC_{lfr}	ΔC_{lLEV}	L	α_{ds}	$\Delta\alpha_{fr}$	$\Delta\alpha_{LEV}$	$\alpha_{①}$	$\alpha_{③}$	$C_{m,min}$	$\Delta C_{m,min}$	M	C_{dmax}	ΔC_{dmax}
Light stall																	
$0° + 15° \sin \omega t$	0.025	1.38	0.46	0.00	0.23	0.23	13.3	13.3	3.3	1.2	8.6	12.0	−0.0175	−0.0135	13.0	0.31	0.248
	0.05	1.48	0.56	0.00	0.38	0.18	14.6	14.6	3.2	1.5	9.8	13.8	−0.020	−0.016	14.2	0.37	0.308
	0.1	1.57	0.65	0.00	0.65	–	14.9	14.9	3.8	–	11.0	14.9_d	−0.0175	−0.0135	14.8	0.37	0.308
	0.2*	–	–	–	–	–	15.0	15.0	3.8	–	11.3	14.7_d	–	–	–	–	–
$5° + 10° \sin \omega t$	0.025	1.33	0.41	0.00	0.20	0.21	13.1	13.1	3.0	1.2	9.0	12.1	−0.016	−0.012	12.0	0.26	0.198
	0.05	1.41	0.49	0.00	0.30	0.19	14.4	14.4	4.0	0.7	10.1	13.9	−0.019	−0.015	13.0	0.34	0.278
	0.1	1.51	0.59	0.00	0.59	–	14.9	14.9	3.2	–	10.6	14.9_d	−0.020	−0.016	14.3	0.36	0.298
	0.2*	–	–	–	–	–	15.0	15.0	3.3	–	10.8	14.7_d	–	–	–	–	–
$10° + 5° \sin \omega t$	0.025	1.30	0.38	0.00	0.20	0.18	14.0	14.0	2.9	0.9	10.2	13.0	−0.012	−0.004	13.1	0.26	0.198
	0.05	1.33	0.41	0.00	0.28	0.13	14.8	14.8	3.2	1.0	10.5	13.8	−0.014	−0.010	13.6	0.30	0.238
	0.1	1.40	0.48	0.00	0.48	–	14.9	14.9	3.0	–	12.0	14.9	−0.015	−0.011	14.7	0.302	0.258
	0.2*	–	–	–	–	–	15.0	15.0	3.2	–	12.2	15.0	–	–	–	–	–
Deep stall																	
$5° + 15° \sin \omega t$	0.025	1.53	0.73	0.17	0.28	0.28	15.2	15.2	4.2	1.8	9.2	13.4	−0.019	−0.015	13.2	0.43	0.368
	0.05	1.70	0.90	0.20	0.37	0.33	18.0	18.0	4.2	3.2	11.6	15.8	−0.025	−0.021	15.0	0.52	0.458
	0.1	2.02	1.22	0.23	0.50	0.49	20.0	20.0	4.2	3.0	12.8	17.0	−0.031	−0.027	17.5	0.77	0.708
	0.2*	–	–	–	–	–	21.4	21.4	4.3	3.1	13.0	18.2	–	–	–	–	–
$10° + 15° \sin \omega t$	0.025	1.47	0.67	0.08	0.34	0.27	17.5	17.5	5.1	2.1	10.5	15.5	−0.0215	−0.0175	15.1	0.425	0.363
	0.05	1.82	1.02	0.10	0.52	0.40	21.1	21.1	6.6	3.0	12.1	17.9	−0.0316	−0.0276	17.5	0.66	0.598
	0.1	2.44	1.52	0.12	0.80	0.59	24.7	24.7	8.4	3.5	12.9	21.1	−0.0395	−0.0350	21.6	0.91	0.823
	0.2*	–	–	–	–	–	23.8_d	23.8_d	9.4	3.6	16.5	24.1_d	–	–	–	–	–
$15° + 15° \sin \omega t$	0.025	1.51	0.71	0.08	0.42	0.21	20.1	20.1	6.1	1.9	12.1	18.2	−0.0196	−0.0156	17.5	0.50	0.438
	0.05	1.83	1.07	0.10	0.49	0.44	24.0	24.0	7.9	3.2	12.9	20.8	−0.0416	−0.0376	20.1	0.75	0.688
	0.1	2.18	1.38	0.15	0.73	0.50	28.7	28.7	8.1	4.7	15.9	24.0	−0.035	−0.031	23.3	1.10	1.038
	0.2*	–	–	–	–	–	28.8	28.8	8.2	4.7	15.9	24.1_d	–	–	–	–	–
$15° + 10° \sin \omega t$	0.025	1.31	0.51	0.05	0.33	0.13	18.6	18.6	4.7	1.9	12.0	16.7	−0.017	−0.013	16.9	0.414	0.352
	0.05	1.66	0.86	0.08	0.42	0.36	21.0	21.0	6.1	2.7	12.2	18.3	−0.026	−0.022	18.3	0.603	0.541
	0.1	1.97	1.17	0.12	0.53	0.52	24.0	24.0	6.3	3.8	13.9	20.2	−0.034	−0.0298	20.2	0.79	0.728
	0.2*	–	–	–	–	–	24.1_d	24.1_d	6.5	4.0	14.3	21.5_d	–	–	–	–	–
$15° + 5° \sin \omega t$	0.025	1.25	0.45	0.09	0.21	0.15	16.9	16.9	3.7	1.0	12.2	15.9	−0.014	−0.010	15.8	0.325	0.263
	0.05	1.43	0.63	0.11	0.28	0.20	18.0	18.0	3.2	2.0	12.8	16.8	−0.017	−0.013	17.0	0.40	0.328
	0.1	1.6	0.8	0.15	0.37	0.28	19.7	19.7	4.9	1.5	13.3	18.2	−0.021	−0.017	18.0	0.51	0.448
	0.2*	–	–	–	–	–	19.1_d	19.1_d	5.0	1.8	13.7	19.9_d	–	–	–	–	–

C_{lmax} = maximum dynamic lift coefficient; ΔC_{lmax} = maximum lift increment = $\Delta C_{lat} + \Delta C_{lfr} + \Delta C_{lLEV}$; $C_{lmax,ss}$ = maximum static lift coefficient; ΔC_{lat} = lift increment due to attached flow effects; ΔC_{lfr} = lift increment due to flow reversal effect; ΔC_{lLEV} = lift increment due to LEV; L = lift stall; α_{ds} = dynamic stall angle; $\Delta\alpha_{fr}$ = angle delayed due to flow reversal effects; $\Delta\alpha_{LEV}$ = angle delayed due to LEV; $\alpha_{①}$ and $\alpha_{③}$ indicate the angles for the occurrence of flow reversal and turbulent separation denoted by points ① and ③ in the dynamic load loops; $C_{m,min}$ = peak dynamic pitching moment coefficient; $\Delta C_{m,max} = C_{m,max} - C_{m,max,ss}$ = maximum pitching moment coefficient variation; $C_{m,max,ss}$ = peak static pitching moment coefficient; M = moment stall angle; $C_{d,man}$ = maximum dynamic drag coefficient; $\Delta C_{d,man} = C_{d,man} - C_{d,man,ss}$ = maximum drag coefficient increment; $C_{dman,ss}$ = maximum static drag coefficient.
Static values: α_{ss} = static-stall angle = 13°; $C_{lmax,ss} = 0.92$; $C_{m,min,ss} = -0.006$; $L = M = 13°$; $C_{dman,ss} = 0.0625$.
* Values obtained from MHFS measurements alone.
^{d} Downstroke.

TABLE 1. Effect of κ, α_m, $\Delta\alpha$ and α_{max} on the critical unsteady aerodynamic values.

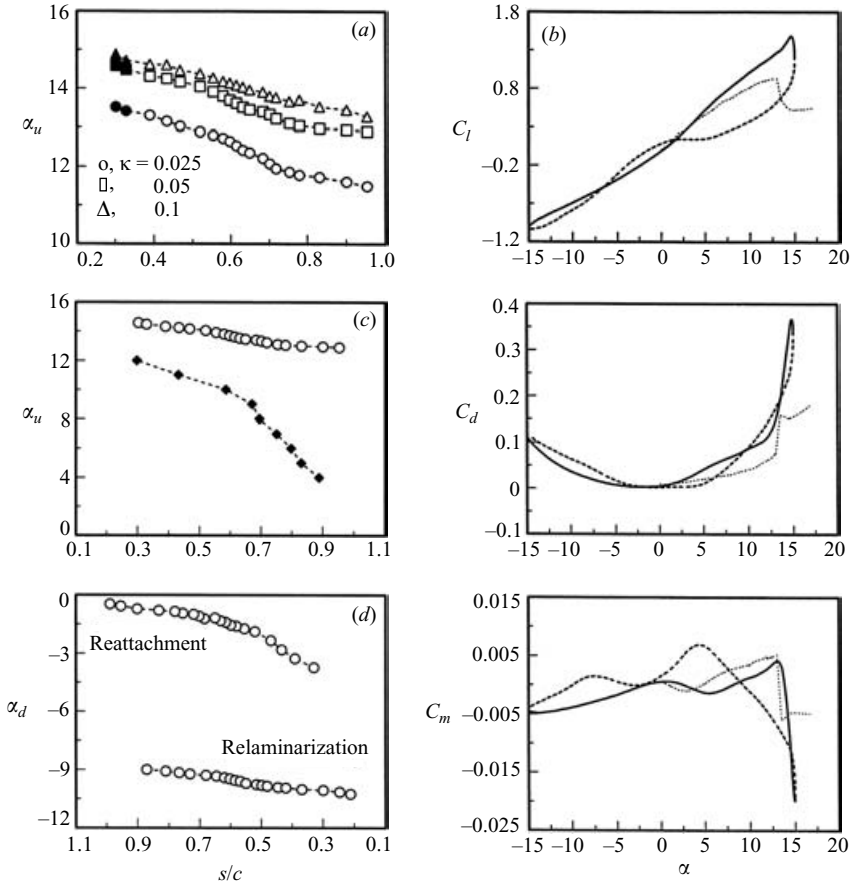

FIGURE 11. Boundary-layer events for $\alpha_m = 0°$ and $\Delta\alpha = 15°$at $\kappa = 0.05$: (*a*) flow reversal and turbulent separation, (*b*) dynamic load loops, (*c*) transition, and (*d*) reattachment and relaminarization. ——, increasing α; · · · ·, decreasing α; · · · ·, static values. Open symbols denote flow reversal and solid symbols turbulent breakdown. ◆, static airfoil.

ratio, thrust coefficient and thrust inclination), which determine stall boundaries for helicopter operations. The results indicate that for a light-stall airfoil, the airfoil stalled from the trailing edge for the range of κ tested, and the extent and abruptness of the separation, however, did not vary considerably. The flow reversal travelled rather rapidly to an uppermost position of $s/c = 0.4$ with increasing α and was followed by a turbulent breakdown at $s/c = 0.3$ (near the top of the oscillation). A vortex-like disturbance of a length of about 30% of c was formed immediately after the turbulent breakdown as the airfoil continued to pitch up. The vortex, however, did not have time to grow and was disrupted as soon as the airfoil pitched through the maximum angle of attack. The rapid trailing-edge stall was found to be responsible for the lift stall.

The various light-stall phenomena described above can be more clearly illustrated from the MHFS signals at $\kappa = 0.05$ (figure 12). The flow reversal and turbulent breakdown are denoted by open and solid triangles, respectively. The existence of the vortex-type disturbance of a length of about 30% of c at $\alpha_u = 14.4°$ was identified from the hot-film signals between S_{118} and S_{87} (or $s/c = 0.0347 - 0.303$). A total lift increment, $\Delta C_{lmax} = 0.56 = \Delta C_{fr} + \Delta C_{lLEV} = 0.38 + 0.18$, and a stall delay of 1.6°

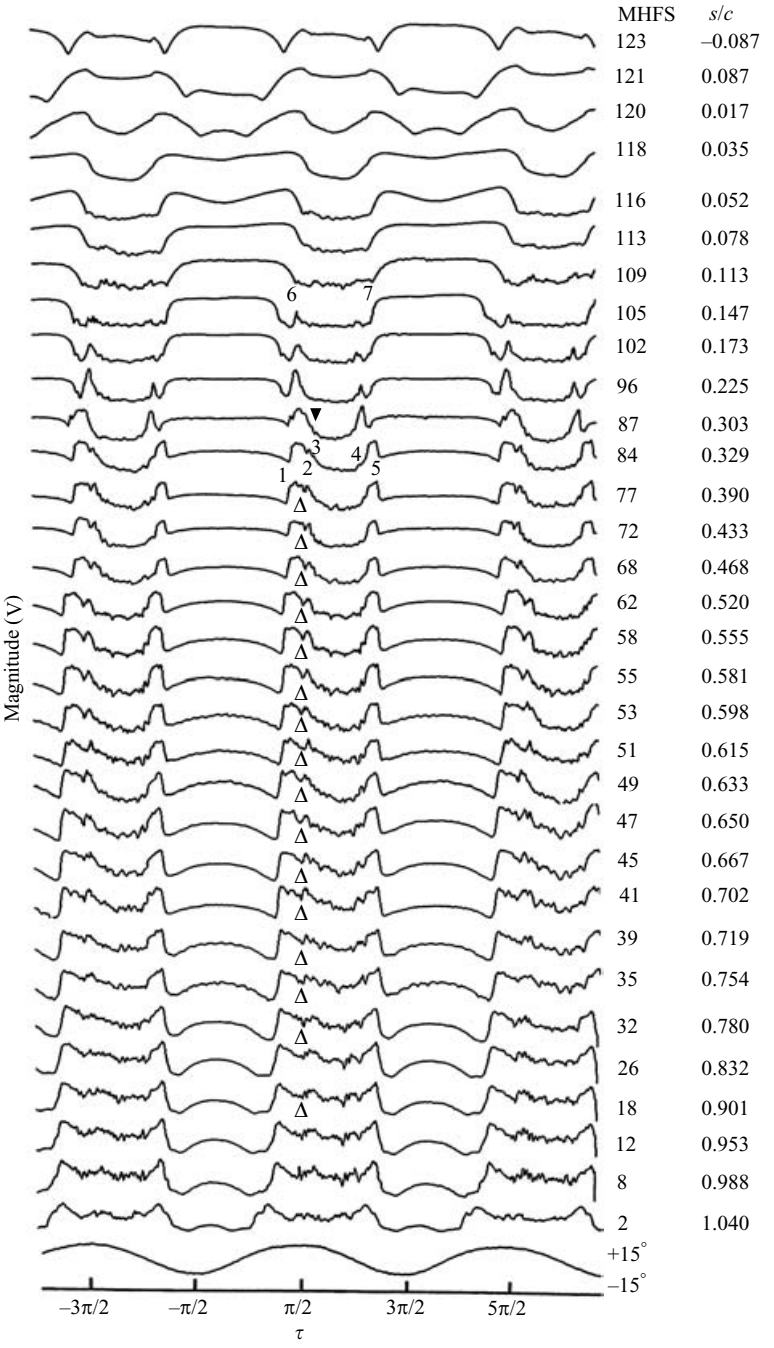

FIGURE 12. Typical MHFS signals for $\alpha(t) = 0° + 15° \sin \omega t$ and $\kappa = 0.05$. △, flow reversal and ▼, turbulent separation. ①, transition, ①–②, attached turbulent boundary layer; ③–④ separated flow; ④ onset of reattachment; ⑤, end of relaminarization.

(i.e. $\alpha_{ds} = 14.6°$; figure 11*b*) were again mainly attributed to the presence and forward movement of the flow reversal, similar to the case of deep-stall airfoil. The LEV, however, did not have enough time to develop and therefore only contributed to

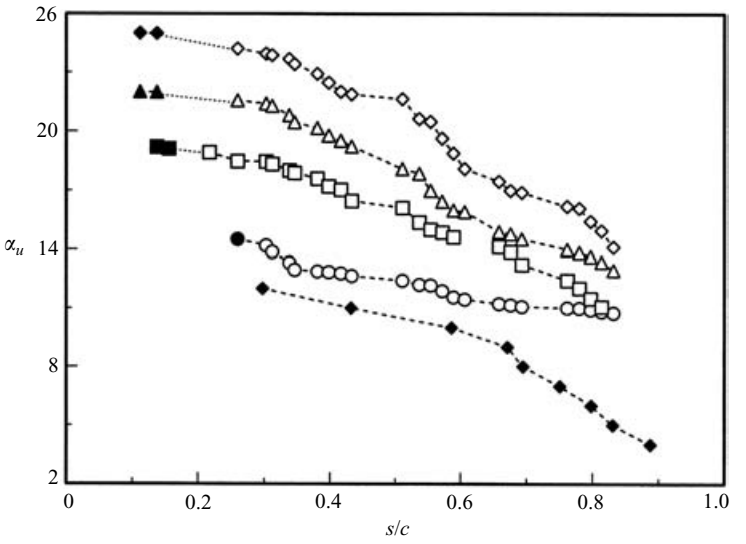

FIGURE 13. Effect of oscillation amplitude on flow reversal (open symbols) and turbulent breakdown (solid symbols) with $\alpha_m = 10^\circ$ and $\kappa = 0.1$. ○, $\Delta\alpha = 5^\circ$; □, 10°; △, 15°; ◇, 20°. ◆, static airfoil.

a smaller increment in lift ($\Delta C_{lLEV} = 0.18$); a large increment in the peak negative pitching moment coefficient $C_{m,min} = -0.02$, however, was observed.

3.2.4. *Effect of oscillation amplitude*

The influence of the maximum incidence α_{max} on the unsteady boundary-layer separation was also investigated (figure 13) by varying the magnitudes of the amplitude $\Delta\alpha$ (= 5°, 10°, 15° and 20°), while keeping the mean angle ($\alpha_m = 10^\circ$) and reduced frequency ($\kappa = 0.1$) constant. As expected, the airfoil exhibited both flow reversal and leading-edge turbulent separation for all the cases studied. However, for $\Delta\alpha = 10^\circ$–20° (i.e. the deep-stall cases), the deep-dynamic stall was consistently characterized by the movement of the flow reversal (up to $s/c = 26\%$) and turbulent separation (at about $s/c = 14\%$), which then led to the formation and the catastrophic detachment of a massive LEV. Similar to the case of reduced frequency, the essential factor involved in these changes was the strength and timing of the dynamic stall vortex, while the positions at which these phenomena were observed remained unaffected by the variation in α_{max}. The deep dynamic stalling mechanism was always of abrupt leading-edge stall type. For the case of $\Delta\alpha = 5^\circ$ (i.e. the light-stall case), the flow reversal moved to an uppermost position of $s/c \approx 40\%$ instead and was followed by a turbulent breakdown at $s/c \approx 30\%$ of c, which rendered the formation of a large premature vortex-like disturbance of about 30% of c as the airfoil continued to pitch up. The dynamic trailing-edge stall was responsible for the observed lift stall. Finally, the effects of amplitude also reflected on the changes in the shape and magnitude in the C_l–C_d–C_m versus α curves (table 1). No significant difference in the maximum values of C_l, C_d and C_m, with the change of oscillation amplitude was observed as long as α_{max} was kept constant.

4. Summary and conclusions

An experimental analysis of the characteristics of the boundary layer and stall events developing on an oscillating NACA 0012 airfoil at $Re = 1.35 \times 10^5$ was conducted.

For an oscillating airfoil, the reduced frequency of the oscillation was found to be highly significant and only small values of reduced frequency were required to delay the onset of the various boundary-layer events, and to produce significant variations in the magnitudes of the peak values of C_l, C_d and C_m. Also, in contrast to a static airfoil, the laminar separation bubble was shortened and only served to cause the transition to turbulence. Brief conclusions are drawn.

(i) For a static NACA 0012 airfoil, the laminar separation and transition, and the trailing-edge flow separation were found to propagate linearly, similar to the linear slope observed in the lift-curve slope, upward but at different rates for $\alpha < 10°$. The static-stalling mechanism was attributed to the bursting of a leading-edge laminar separation bubble.

(ii) For deep-stall oscillations, the prior-to-stall boundary-layer conditions were dominated by the approximated linear upward spread of a flow reversal (always up to an uppermost of $s/c = 0.26$) and the sudden turbulent breakdown at around $s/c = 0.14$, and the subsequent formation, growth and convection of an energetic leading-edge vortex, which contributed to the observed significant increase in the C_l, C_d and C_m values. The LEV and the secondary vortex always spread rearward at 45% of u_∞ and 30% of u_∞, respectively, insensitive to the reduced frequency, suggesting that no 'LEV-trapping advantage' was realized by changing the reduced frequency. The post-stall condition was featured by the reattachment of the separated flow and the subsequent return of the boundary layer to the laminar state for the rest of the oscillation cycle. There was a significant hysteresis in the phases and the angles of attack between the unsteady flow separation and reattachment points. The lift stall occurred when the LEV reached 90% of the chord, while the moment stall occurred at the end of the upward spread of the trailing-edge flow reversal. Moreover, the leading-edge dynamic stall was found not to originate with the bursting of a laminar separation bubble, as is commonly believed, but with a sudden turbulent breakdown at a short distance downstream of the leading edge.

(iii) For the light-stall oscillating case, the flow reversal persisted up to 40% of chord downstream of the leading edge, and was followed by a turbulent breakdown at around 30% of chord as the airfoil continued to pitch up to the top of the oscillation, causing the formation of a vortex like disturbance or circulation region of length of about 30% of the chord length. The vortex did not have time to grow and was swept away by the airfoil pitch-down motion. The lift stall was characterized by the rapid trailing-edge dynamic stall.

(iv) For attached-flow oscillating case, the boundary-layer transition and its return to laminar flow were delayed and promoted, respectively, in a nonlinear manner, relative to the static case, when the incidence was increasing and decreasing. The aerodynamic forces and pitching moment followed the general trends of those of a static airfoil, but with a slight improvement in the lift coefficient and the lift-curve slope.

This work was supported by the Natural Sciences and Engineering Research Council (NSERC) of Canada. G. Petrakis is thanked for his help on the design of the oscillation mechanism.

REFERENCES

Bisolinghoff, R. L. & Ashley, H. 1975 *Principles of Aeroelasticity*. Dover.

Carr, L. W., McAlister, K. W. & McCroskey, W. J. 1977 Analysis of the development of dynamic stall based on oscillating airfoil experiments. *NASA TN* D-8382.

Chandrasekhara, M. S. & Carr, L. W. 1990 Flow visualization studies of the Mach number effects on dynamic stall of an oscillating airfoil. *J. Aircraft* **27**, 516–522.

Chen, S. H. & Ho, C. M. 1988 Near wake of an unsteady airfoil. *J. Fluids Structures* **1**, 151–164.

Chow, C. Y. & Chiu, C. S. 1986 Unsteady loading on an airfoil due to vortices released intermittently from its surface. *J. Aircraft* **23**, 750–755.

Desgeorges, O. & Lee, T. 2002 Calibration of multiple hot-film sensor arrays and skin friction measurement. *Exps. Fluids* **32**, 37–43.

Ericsson, L. E. & Reding, J. P. 1988 Fluid mechanics of dynamic stall. Part I. Unsteady flow concept. *J. Fluids Structures* **2**, 1–33.

Greenblatt, D., Neuburger, D. & Wygnaski, I. 2001 Dynamic stall control by intermittent periodic excitation. *J. Aircraft* **38**, 188–190.

Hsiao, F. B., Liang, P. F. & Huang, C. Y. 1998 High-incidence airfoil aerodynamics improvement by leading-edge oscillating flap. *J. Aircraft* **35**, 508–510.

Johnson, W. & Ham, N. D. 1972 On the mechanism of dynamic stall. *J. Am. Helicopter Soc.* 36–45.

Jumper, E. J. 1988 Toward an unsteady flow airplane. *AIAA Paper* 88-0752.

Jumper, E. J., Dimmick, R. L. & Allaire, A. J. S. 1989 The effect of pitch location on dynamic stall. *J. Fluids Engng* **111**, 256–262.

Jumper, E. J., Schreck, S. J. & Dimmick, R. L. 1987 Lift-curve characteristics for an airfoil pitching at constant rate. *J. Aircraft* **24**, 680–687.

Ko, S. & McCroskey, W. J. 1997 Computations of unsteady separating flows over an oscillating airfoil. *AIAA J.* **35**, 1235–1238.

Lee, T. 1999 Investigation of unsteady boundary layer developed on a rotationally oscillating circular cylinder. *AIAA J.* **37**, 328–336.

Lee, T. & Basu, S. 1997 Nonintrusive measurement of boundary layers developed on a single and two tandem circular cylinders. *Exps. Fluids* **23**, 187–193.

Lee, T. & Basu, S. 1998 Measurement of unsteady boundary layer developed on an oscillating airfoil using multiple hot-film sensors. *Exps. Fluids* **25**, 108–117.

Lee, T. & Birch, B. 2004 The structure and induced drag of a tip vortex. *J. Aircraft* **41**(4) (to appear).

Lober, P. F., Carta, F. O. & Covino, A. F. 1992 An oscillating three-dimensional wing experiment: compressibility, sweep, rate, and geometry effects on unsteady separation and dynamic stall. *United Technologies Research Center Rep.* R92-958325-6. East Hartford, Connecticut, USA.

McAlister, K. W., Carr, L. W. & McCroskey, W. J. 1978 Dynamic stall experiments on the NACA 0012 airfoil. *NASA TP* 1100.

McCroskey, W. J. 1982 Unsteady airfoils. *Annu. Rev. Fluid Mech.* **14**, 285–311.

McCroskey, W. J., McAlister, K. W., Carr, L. W., Pucci, S. L., Lamber, O. & Indergrand, R. F. 1981 Dynamic stall on advanced airfoil sections. *J. Am. Helicopter Soc.* **26**, 40–50.

McCroskey, W. J., Carr, L. W. & McAlister, K. W. 1976 Dynamic stall experiments on oscillating airfoils. *AIAA J.* **14**, 57–63.

McCroskey, W. J. & Philippe, J. J. 1975 Unsteady viscous flow on oscillating airfoils. *AIAA J.* **13**, 71–79.

Magill, J., Bachmann, M., Rixon, G. & McManus, K. 2003 Dynamic stall control using a model-based observer. *J. Aircraft* **40**, 355–362.

Martin, J. M., Empey, R. W., McCroskey, W. J. & Caradonna, F. X. 1974 An experimental analysis of dynamic stall on an oscillating airfoil. *J. Am. Helicopter Soc.* 26–32.

Nguyen, K. 1998 Active control of helicopter blade stall. *J. Aircraft* **35**, 91–98.

Panda, J. & Zaman, B. M. Q. 1994 Experimental investigation of the flow field of an oscillating airfoil and estimation of lift from wake surveys. *J. Fluid Mech.* **265**, 65–95.

Park, S. O., Kim, J. S. & Lee, B. I. 1989 Hot-wire measurements of near wakes behind an oscillating airfoil. *AIAA J.* **28**, 22–28.

Rennie, R. M. & Jumper, E. J. 1996 Experimental measurements of dynamic control surface effectiveness. *J. Aircraft* **33**, 880–887.

Schreck, S., Faller, W. & Helin, H. 1994 Pitch rate and Reynolds number effect on unsteady boundary layer transition and separation. *AIAA Paper* 94-2256.

Srinivassan, G. R., Ekaterinaris, J. A. & McCroskey, W. J. 1993 Dynamic stall of an oscillating wing. Part 1: Evaluation of turbulence models. *AIAA Paper* 93-3403.